

Graphene-based Josephson Junctions: Phase Diffusion,  
Effects of Magnetic Field, and Mesoscopic Properties.

by

Ivan V. Borzenets

Department of Physics  
Duke University

Date: \_\_\_\_\_

Approved:

---

Gleb Finkelstein, Supervisor

---

Harold Baranger

---

Stephen Teitworth

---

Ashutosh Kotwal

---

Jungsang Kim

Dissertation submitted in partial fulfillment of the requirements for the degree of  
Doctor of Philosophy in the Department of Physics  
in the Graduate School of Duke University  
2012

ABSTRACT

Graphene-based Josephson Junctions: Phase Diffusion,  
Effects of Magnetic Field, and Mesoscopic Properties.

by

Ivan V. Borzenets

Department of Physics  
Duke University

Date: \_\_\_\_\_

Approved:

---

Gleb Finkelstein, Supervisor

---

Harold Baranger

---

Stephen Teitworth

---

Ashutosh Kotwal

---

Jungsang Kim

An abstract of a dissertation submitted in partial fulfillment of the requirements for  
the degree of Doctor of Philosophy in the Department of Physics  
in the Graduate School of Duke University  
2012

Copyright © 2012 by Ivan V. Borzenets  
All rights reserved except the rights granted by the  
Creative Commons Attribution-Noncommercial Licence

# Abstract

We report on graphene-based Superconductor-Normal metal-Superconductor Josephson junctions with contacts made from lead. The high transition temperature of this superconductor allows us to observe the supercurrent branch at temperatures up to  $\sim 2$  K. We are able to detect a small, but non-zero, resistance despite the Josephson junctions being in the superconducting state. We attribute this resistance to the phase diffusion regime, which has not been yet identified in graphene. By measuring the resistance as a function of temperature and gate voltage, we can further characterize the nature of electromagnetic environment and dissipation in our samples. In addition we modulate the critical current through graphene by an external magnetic field; the resulting Fraunhofer interference pattern shows several periods of oscillations. However, deviations from the perfect Fraunhofer pattern are observed, and their cause is explained by a simulation that takes into account the sample design.

I dedicate this work to my parents and grandparents who taught me that education is a life long process.

# Contents

<b>Abstract</b>	<b>iv</b>
<b>List of Figures</b>	<b>ix</b>
<b>List of Abbreviations and Symbols</b>	<b>xi</b>
<b>Acknowledgements</b>	<b>xii</b>
<b>1 Introduction</b>	<b>1</b>
1.1 Josephson Junction . . . . .	1
1.2 Graphene . . . . .	2
1.3 Graphene-based Josephson Junctions . . . . .	2
<b>2 Graphene Overview</b>	<b>4</b>
2.1 Graphene Basics . . . . .	4
2.2 Synthesis . . . . .	5
2.3 Band Structure . . . . .	6
<b>3 Review of Josephson Junction</b>	<b>10</b>
3.1 Josephson Junction . . . . .	10
3.2 RCSJ Model . . . . .	11
3.3 Phase Diffusion . . . . .	15
3.4 Effects of Magnetic field . . . . .	20
3.5 SNS . . . . .	20
3.6 Graphene based SNS Josephson junctions . . . . .	23

<b>4</b>	<b>Sample Preparation</b>	<b>26</b>
4.1	Graphene Deposition . . . . .	26
4.2	Graphene Characterization . . . . .	29
4.3	Lithography . . . . .	31
4.4	Lead Deposition . . . . .	32
<b>5</b>	<b>Measurement Setup</b>	<b>37</b>
5.1	Overview . . . . .	37
5.2	Room Temperature Electronics . . . . .	39
5.2.1	Current Source . . . . .	39
5.2.2	Voltage Amplifier . . . . .	41
5.2.3	Gate . . . . .	45
5.3	Cryostat Specific Electronics . . . . .	48
5.3.1	Variable temperature probe . . . . .	48
5.3.2	Dilution Fridge . . . . .	48
<b>6</b>	<b>Critical Current and Phase Diffusion</b>	<b>52</b>
6.1	Introduction . . . . .	52
6.2	Quick Review and Sample Parameters . . . . .	53
6.3	Critical Current and Phase Diffusion . . . . .	54
6.4	Application of Small B-Fields and Quality factor analysis . . . . .	60
<b>7</b>	<b>Non-trivial Effects of Magnetic Field</b>	<b>63</b>
7.1	Sample and Measurement Design . . . . .	63
7.2	Results . . . . .	66
7.3	Simulation . . . . .	69
<b>8</b>	<b>Conclusion and Future plans</b>	<b>72</b>
8.1	Conclusion . . . . .	72

8.2 Future measurements . . . . .	73
<b>Bibliography</b>	<b>75</b>
<b>Biography</b>	<b>79</b>

# List of Figures

2.1	Schematic representation of graphene . . . . .	5
2.2	Band structure of graphene . . . . .	7
2.3	Graphene puddles. . . . .	8
3.1	Schematic of a conventional Josephson junction. . . . .	11
3.2	Schematic of an RCSJ junction . . . . .	12
3.3	RCSJ model washboard potential. . . . .	13
3.4	Representation of a switching and retrapping measurement. . . . .	14
3.5	Underdamped junction versus the Phase Diffusion regime. . . . .	17
3.6	Switching current versus temperature . . . . .	18
3.7	Fraunhofer interference pattern. . . . .	19
3.8	Superconductor-Normal metal- Superconductor schematic. . . . .	21
3.9	SNS $I_C$ v.s. $E_{Th}$ relationship at $T = 0$ . . . . .	22
3.10	$T$ dependence of $I_C$ in an SNS junction. . . . .	23
3.11	Graphene based SNS junctions. . . . .	24
4.1	Image of a graphene flake. . . . .	28
4.2	2D peak vs number of layers. . . . .	30
4.3	Raman spectrum of our graphene sample . . . . .	31
4.4	SEM micrograph of superconducting contacts. . . . .	33
4.5	SEM micrograph of an old graphene sample. . . . .	35
5.1	Measurement system schematic. . . . .	38

5.2	Current source. . . . .	40
5.3	Chip based voltage amplifier. . . . .	42
5.4	Transistor based voltage amplifier. . . . .	44
5.5	Commercial amplifier. . . . .	45
5.6	Schematic of the gate amplifier. . . . .	47
5.7	Low temperature passive filters. . . . .	49
5.8	Dilution fridge cold finger. . . . .	51
6.1	Current-Voltage characteristic . . . . .	55
6.2	Switching and Retrapping Currents . . . . .	56
6.3	Phase Diffusion . . . . .	58
6.4	Damping Analysis . . . . .	61
7.1	Magnetic field measurement setup . . . . .	64
7.2	Magnetic field v.s. Temperature . . . . .	65
7.3	Interference pattern distortions . . . . .	67
7.4	Trapped Flux . . . . .	68
7.5	Simulation . . . . .	70
7.6	Large B-Field sweep . . . . .	71

# List of Abbreviations and Symbols

## Abbreviations

SNS	Superconductor-Normal metal-Superconductor Josephson junctions
SGS	Superconductor-Graphene-Superconductor Josephson junctions
SEM	Scanning electron microscope
B-Field	Magnetic field.
HOPG	Highly oriented pyrolytic graphite
CVD	Chemical vapor deposition
RCSJ	Resistively and Capacitively Shunted junction
Pb	Lead
Pd	Palladium
Cr	Chromium
Au	Gold
PMMA	Poly(methyl methacrylate)
DAC	Digital to analog converter
JFET	Junction gate field-effect transistor
RC	Resistance, capacitance passive filter
RF	Radio Frequency
op-amp	Operational Amplifier
$I - V$	Current- voltage characteristic

# Acknowledgements

First and foremost I would like to thank Prof. Gleb Finkelstein for his mentorship and guidance through the entire Ph.D. process. I would like to thank my fellow lab members: Dr. Yuri Bomze for his valuable skills and knowledge of electronics and cryogenics systems, Dr. Ulas Coskun for introducing me to graphene, and supplying a lot of the graphene flakes used for measurement, Dr. Henok Mebrahtu for his aid in sample preparation. All of my lab mates were valuable research collaborators, great aids when it came to classwork, and are now irreplaceable friends.

I would also like to thank the fellow theory group headed by Prof. Harold Baranger, who was a great instructor, and provided useful and timely input and suggestions related to our measurements. Abhijit Mehta, a student of Prof. Baranger was especially helpful in discussing the measured data as it was arriving. He has become a close friend over the years.

Finally, I would like to thank Prof. Alex Smirnov of the North Carolina State University for providing access to equipment which allowed for lengthy and detailed measurement on our sample.

I would like to acknowledge Duke University, and specifically the Physics Department for supporting me through the Ph.D. process. The Sharer Materials Instrumentation Facility (SMIF) for providing sample preparation and characterization equipment, as well as valuable training.

The work was supported by the U.S. Department of Energy, Office of Basic

Energy Sciences, Division of Materials Sciences and Engineering under Award DE-SC0002765.

Lastly I appreciate valuable discussions with Sergei Tolpigo, Timur Filippov, D.V. Averin, M.V. Feigelman, V.B. Geshkenbein, S. Gueron, P.J. Hakonen, N.B. Kopnin, J.P. Pekola, and V.S. Shumeiko.

# Introduction

## 1.1 Josephson Junction

The phenomenon of superconductivity has been first discovered in 1911(1), yet even today the subject is of great interest for many academic groups as well as industry. Significant early achievements in studying superconductivity have been made by Duke University's own Fritz London(2). The advances made by theoretical physicists in describing the laws governing superconductivity are by many considered to be the most successful application of the field of condensed matter physics.

In the heart of the majority of studies involving superconductivity lies the device known as a Josephson junction(3). A Josephson junction in its basic form is two superconducting leads separated by another material: insulator, metal, semiconductor, even a different superconductor, or a combination of several such materials. It has been found that despite the resistive properties of the materials separating the two superconducting leads, it is possible for quite a large electrical current to flow through a Josephson junction without developing a voltage.

Devices made from Josephson junctions have been used to create ultra sensitive

sensors (especially magnetic field sensors), classical digital electronics which feature both high frequencies and low power dissipation, and more recently, quantum electronics. Josephson junction still attract significant attention in their use as imaging sensors(4) as well as their potential utilization in quantum computing(5).

## 1.2 Graphene

A single atomic layer of graphite is known as graphene. It is considered by many to be the most basic state of crystalized carbon and is the building block for more complex carbon structures such as nanotubes and fullerenes. Graphene has been studied theoretically since the 1940's(6), but has only been experimentally isolated in 2004(7). Since then, there has been an explosion of interest in the physical properties of graphene as well as its potential applications(8).

Graphene's low defect crystalline form allows for very high electron mobilities, meaning that it is an attractive material for creating novel, high speed, digital devices. At the same time, graphene is only a single atomic layer thick, transparent in the visible spectrum, is extremely flexible yet very durable. These properties open up many potential applications for graphene; from the most basic such as its use in window defrosters, to the more complex uses of making flexible and transparent electronics such as a video screen that can be folded to fit into a pocket(9).

## 1.3 Graphene-based Josephson Junctions

It has been shown that a sheet of graphene can act as the material that separated two superconductors in a Josephson junction. Such a device is know as a graphene-based, Superconductor-Normal metal-Superconductor Josephson junction, or SGS Josephson junction. The gate tunability of graphene as well as its two dimensional nature opens up much additional potential of Josepshon junction devices. We characterize and study several such devices. First, we devise a method of using lead

(Pb) as the superconducting material in the graphene-based Josephson junction, thus increasing the temperature at which a supercurrent can be seen through such a junction. The higher temperature and better thermalization of our devices eliminates the overheating effect commonly associated with such Josephson junctions. The lack of overheating allows us to conclude that our junctions are underdamped, a rare condition in Superconductor-Normal metal-Superconductor type Josephson junctions. In addition, the higher temperatures at which the supercurrent appears, allows us to observe the phase diffusion regime(2), the analysis of which we find to be in good agreement with theory. Finally, we look at the magnetic modulation of the critical current in our junctions and we observe a deviation from standard theory. We explain these deviations by the unusual sample design which is somewhat uniquely associated with the use of graphene.

## Graphene Overview

### 2.1 Graphene Basics

The most common form of carbon is graphite, which is a crystal composed of sheets (or layers) of SP-2 bonded carbon. Each layer is a planar honeycomb structure of strongly bonded carbon atoms, where each atom forms a sigma bond with three adjacent atoms. While the bonding of atoms within a single layer is strong, a stack of these sheets is loosely bound and can easily be cleaved. A single, isolated sheet of SP-2 bonded carbon is known as Graphene(8).

As such, graphene is the basic form for most carbon based structures: multiple sheets of graphene form graphite, a sheet of graphene rolled into a cylinder forms a nanotube, and a sheet of graphene curved in such a way as to completely enclose a volume is a fullerene. The properties of graphene have been studied since 1947(6), however experimentally a single atomic layer of graphene has only been isolated in 2004(7).

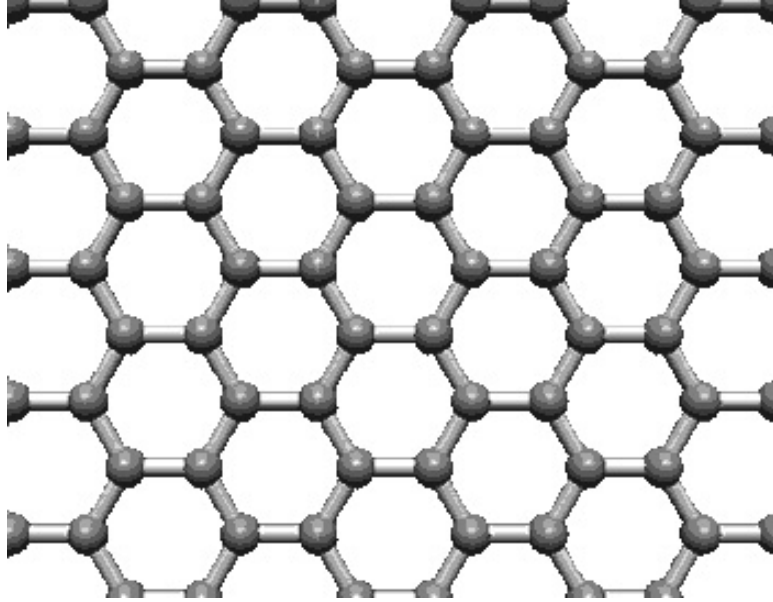


FIGURE 2.1: A schematic representation of a graphene crystal. Graphene is a two dimensional crystalline sheet of SP-2 bonded carbon (each carbon atom bonds to three others in plane). Since each carbon atom has four valence electrons, but is bonded to only 3 other atoms, the last electron is equally shared among all the bonds and is free to "hop" between atoms and is the source of conductivity in graphene. Since the atomic bonding is all in a single plane, graphene has good thermal and electrical conductivity in the plane of the crystal, however a stack of several graphene layers is loosely bound and has poor conductive properties between layers.

## 2.2 Synthesis

The original, and still the most common method for isolating a single sheet of graphene is known as mechanical exfoliation(7). A crystal of natural graphite or highly oriented pyrolytic graphite (HOPG) is used as a source. Thin sheets of graphite are cleaved from a bulk crystal by placing an adhesive tape over the crystal and peeling it off. This tape containing few layers of graphite is then pressed onto or rubbed over a very clean silicone substrate. Since individual layers of graphite are adhered very loosely to each other, some of them will detach from the bulk and instead attach to the surface of the silicone substrate. It is possible that only a single layer of carbon will transfer onto the surface. This method is straightforward, and produces very

high quality graphene with low defects. However, since it is impossible to predict where on the substrate a flake of graphene will be deposited (if at all), this method is not scalable and is therefore limited to research applications.

Several methods have been developed to "grow" a macroscopic sheet of graphene. Using these methods, it is possible to cover an entire silicon substrate wafer with graphene and later pattern it into devices as desired. This allows for the potential integration of graphene in industrial devices. The most notable method is chemical vapor deposition (CVD) growth of graphene on copper or nickel foil(10). The atomic structure of the metal foil acts as a seed on top of which carbon grows epitaxially in a crystalline pattern. The carbon atoms are introduced from a source gas (usually methane) at a high temperature. The resulting graphene sheets can be as big as  $1m^2$  in area(9). The graphene can be easily removed from the copper film it was grown on, and transferred to any desired substrate. However, graphene that has been grown by the CVD method is of much lower quality compared to the flakes deposited using mechanical exfoliation. The loss of quality is attributed to random lattice defects and to the graphene simultaneously growing from several nucleating points, thus forming misaligned domains.

### 2.3 Band Structure

Graphene is a gapless semiconductor(6). The energy-momentum relation linearly (or conically) goes to zero at six points (two inequivalent) in the Brillouin zone:  $E = \hbar V_f \sqrt{k_x^2 + k_y^2}$ . Here  $k_x$  and  $k_y$  is the relative momentum and  $V_f \sim 10^6 m/s$  is the Fermi velocity(11; 12). This unique linear energy-momentum dispersion implies that at low energies the electrons in graphene behave as massless, Dirac fermions. As such, the points of momentum (as well as the value of gate voltage) at which the energy goes to zero are known as Dirac points. At the Dirac point, the charge carrier concentration goes to zero, and therefore the graphene sheet becomes insu-

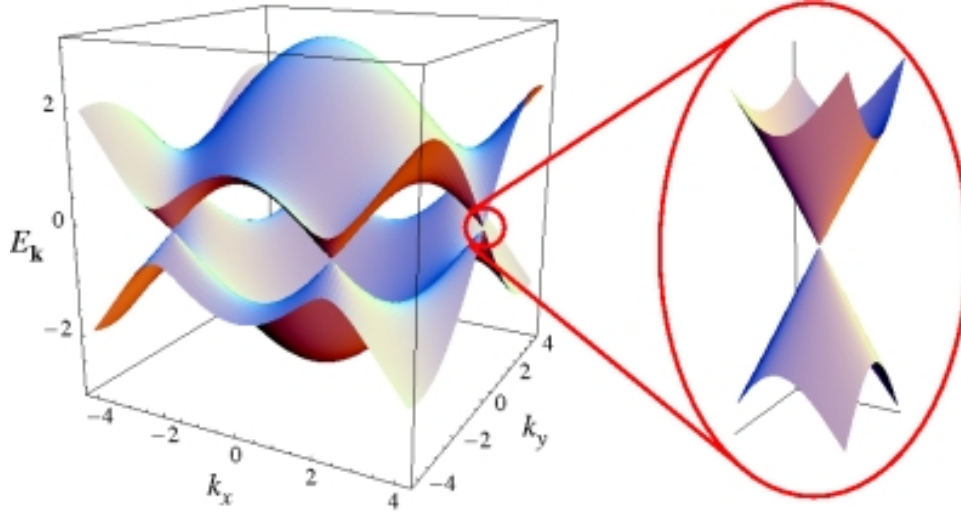


FIGURE 2.2: Energy-momentum relation for an ideal graphene sheet(14). One can see that for several values of momentum in the Brillouin zone the energy goes to zero. Moreover, for small values of energies around those points, the energy-momentum relation is linear (or conical).  $E = \hbar V_f \sqrt{k_x^2 + k_y^2}$  (The variables from momentum  $k_x$  and  $k_y$  are of course relative to that special point where the energy goes to zero. Due to this linear dispersion relation, the electrons behave as massless, Dirac fermions. As such the points where energy goes to zero are known as Dirac points, and the energy-momentum relation for low energies is called the Dirac cone. One can use a gate voltage to change the Fermi level in a graphene crystal, and is therefore, able to sweep the energy through the Dirac cone.

lating. At high concentration of carriers, graphene has been found to have extremely high electron mobilities theoretically capped at room temperatures as  $2 * 10^5 \text{cm}^2/\text{Vs}$  corresponding to a resistivity of  $10^{-6} \Omega \text{cm}$ , lower than the resistivity of silver(13).

In an ideal crystal of graphene, the charge carrier concentration goes to zero when the Fermi energy is tuned to the Dirac point, implying that graphene will become insulating. However, experimentally this is found not to be the case. It has been found that the electrons and holes in graphene are not uniformly distributed, but instead form puddles (alternating areas of large concentration of electrons and holes)(15). The non-uniform carrier distribution is attributed to the random electronic potential typically attributed to lattice defects in the graphene crystal, the curvature (rippling)

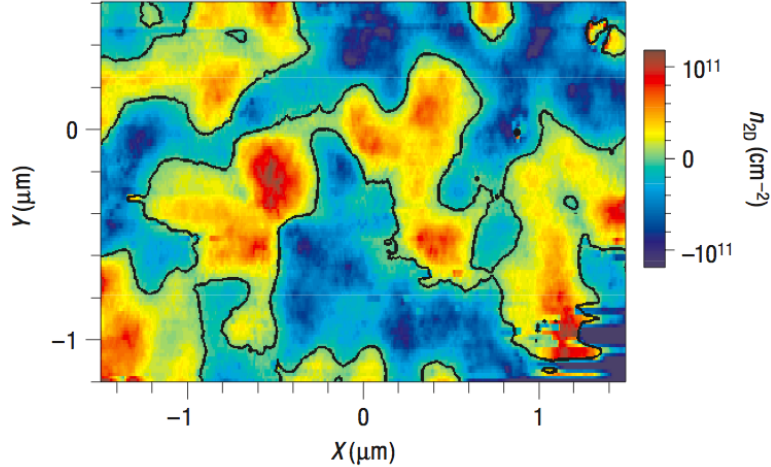


FIGURE 2.3: Shown here is a scanning measurement of the spacial distribution of carrier concentration in a graphene flake (experiment by Yacoby et. al.)(15). The blue regions correspond to areas of large net hole concentrations, the red regions correspond to areas where there is a large electron concentration. The black contour is the line where the charge carrier concentration is zero. This map was taken when the graphene flake adjusted to have the Fermi level at the Dirac point, therefore, having an average zero carrier concentration. However, impurities (such as charged particles above and below the graphene sheet) locally gate the graphene. This locally shifts the Fermi level and the carrier concentration creating electron or hole "puddles". The non-uniform distribution of charge carrier results in non-zero conductance through the graphene sheet even though in an ideal crystal the carrier concentration is zero at the Dirac point. In addition to non-zero conductance, the existence of "puddles" effectively widens the Dirac cone in gate voltage. A high concentration of impurities in/on a graphene crystal can destroy the gate dependence entirely.

of the graphene sheets, and more importantly charged particles that lie on the surface of the graphene crystal. Therefore, there is no value of gate voltage where the carrier concentration goes to zero over the entire graphene crystal. In addition, it has been shown that relativistic Dirac fermions, such as the charge carriers in graphene, will have a surprisingly high tunneling rate across high potential barriers(16). This phenomenon allows for transport between the puddles in graphene.

The charged particles typically contaminate graphene during the process of exfoliation, deposition, and and lithography. This contamination locally gates the

graphene crystal and as a result widens the gate dependence of conductivity and moves the Dirac point of graphene away from zero gate voltage. Highly contaminated samples lose their gate dependence entirely. In order to clean the graphene crystal, it is usually annealed at several 1000 degrees as the final processing step before measurement. Sometimes, the substrate underneath the graphene crystal is etched away, thus resulting in suspended graphene. When annealed, suspended graphene can be cleaned from charged contamination on both the top and bottom surfaces(17). However, if the electrical contacts to graphene are made from soft metals, as in our case, annealing of the sample would damage the contacts and therefore cleaning of graphene becomes a challenge.

## Review of Josephson Junction

### 3.1 Josephson Junction

The device made from two superconducting electrodes separated by a thin insulating layer (typically few nm thick) is known as an (SIS) Josephson junction(3; 2). Despite being highly resistive at room temperature, it has been predicted (3) as well as experimentally confirmed that below the critical temperature of the superconducting electrodes, such junctions are able to support a zero-voltage supercurrent of  $I = I_C \sin(\Delta\phi)$ . Where  $I_C$  is the critical current (the maximum current that can flow through the junction while still maintaining zero voltage) and  $\Delta\phi$  is the difference in phase of the Ginsbug-Landau wavefunction of the superconducting electrodes. The critical current of the junction can be expressed as Josephson energy  $E_J = \hbar I_C / 2e$ . This Josephson energy is the measure of the coupling strength of the phases of the two superconducting electrodes, and depends on the thickness and material of the insulating layer. However, a time evolution of the phase difference between the superconducting electrodes results in a non-zero voltage across the junction  $\frac{d\Delta\phi}{dt} = \frac{2eV}{\hbar}$ .

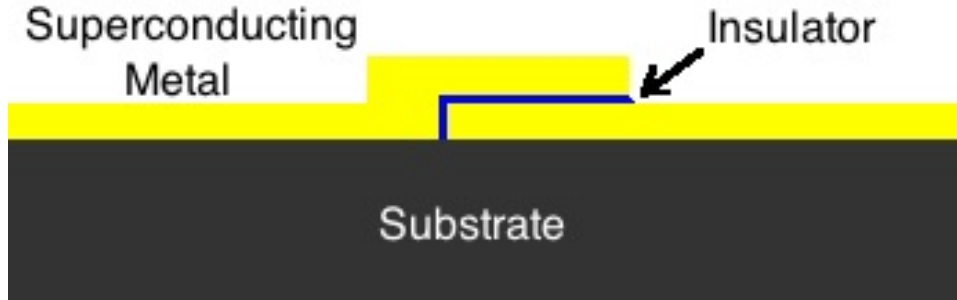


FIGURE 3.1: A schematic representation of a Superconductor-Insulator-Superconductor (SIS) Josephson junction. The schematic is a cut along the vertical axis of a typical SIS Josephson junction design. Two superconducting metal leads are separated by an insulating layer. The thickness of this layer is typically of the order of less than one nm, so as to create a tunneling junction. However, at temperatures below the critical transition temperature  $T_C$  of the superconducting leads, the junction is able to support a supercurrent of up to  $I_C$  without developing a voltage.

### 3.2 RCSJ Model

A more accurate model of the Josephson junction is provided by the RCSJ (Resistively, Capacitively Shunted Junction) model(2). This model approximates a real world junction by an ideal Josephson junction, a resistor and a capacitor all connected in parallel. The capacitor has a value equal to the capacitance  $C$  between the two superconducting electrodes. For SIS Josephson junctions, the shunting resistor  $R$  is the quasiparticle resistance of the junction which has the value of the normal resistance  $R_N$  at the transition temperature  $T_C$  and increases with lower temperature as  $R_{QP} = R_n \exp(\Delta/k_B T)$ . ( $\Delta$  is the superconducting gap.) The current flowing through the junction is the sum of the currents flowing through each element  $I = I_C \sin(\phi) + \frac{V}{R} + C \frac{dV}{dt}$ . We convert voltages to time evolution of phase ( $\frac{d\Delta\phi}{dt} = \frac{2eV}{\hbar}$ ), and define a plasma frequency  $\omega_P = \sqrt{2eI_C/\hbar C}$  which allows us to change time to a dimensionless variable  $\tau = \omega_P t$ . Thus the current through our junction becomes  $I = I_C(\sin(\phi) + 1/Q \frac{d\phi}{d\tau} + \frac{d^2\phi}{d\tau^2})$ , where  $Q = \omega_P RC$  is known as the quality factor. This differential equation is analogous to that of a particle moving

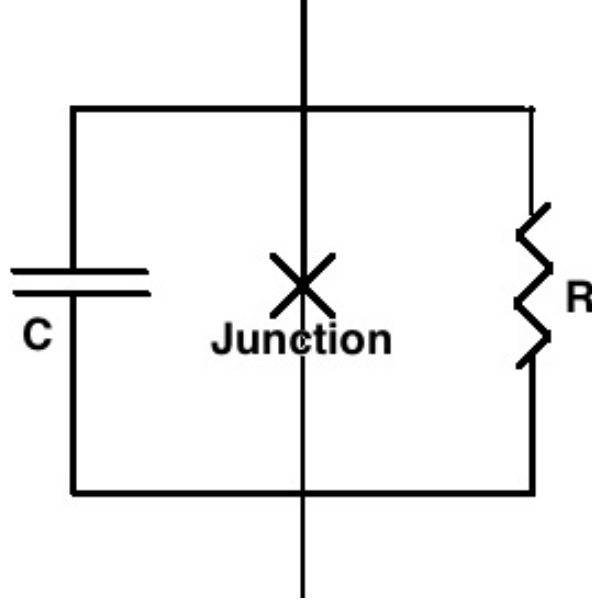


FIGURE 3.2: Shown here is a circuit representation of the Resistively and Capacitively Shunted Junction (RCSJ) model for a realistic SIS Josephson junction. The Josephson junction itself consists of an ideal junction shunted by a resistor and a capacitor. The shunting capacitor is the capacitance between the two superconducting electrodes of the junction, while the shunting resistance is typically the quasiparticle resistance  $R_{QP}$ .

in a potential  $U(\phi) = -E_J \sin(\phi) - \frac{\hbar I}{2e} \phi$ , known as the "washboard potential". At zero bias current, the system is contained in a local potential well of energy  $E_J$ . In this state, the change in phase  $\frac{d\phi}{dt}$  averages to zero and no voltage is seen. As the bias current is increased, the potential becomes tilted and the barrier of the well is lowered. When the critical current  $I_C$  is reached, the washboard potential is tilted to the point where local minimum becomes an inflection point and the phase can be no longer contained but must continuously change time, corresponding to the normal regime. At non zero temperatures, thermal noise can excite the system with enough energy to overcome the potential barrier before the critical current is reached. How a system behaves in when thermal noise becomes a factor depends on the junction's quality factor  $Q$ .

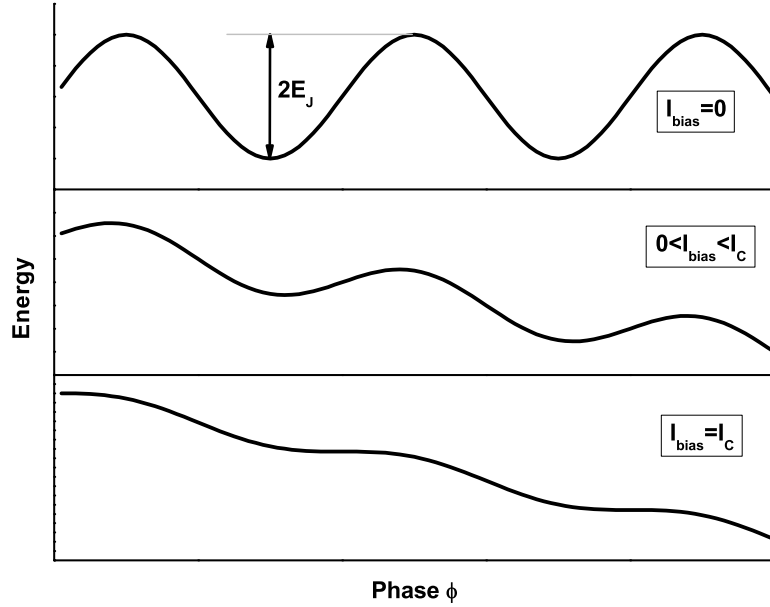


FIGURE 3.3: The RCSJ model of a Josephson junction reduces to that of a motion of a particle in a potential  $U(\phi) = -E_J \sin(\phi) - \frac{\hbar I}{2e} \phi$ , known as the washboard potential. Here,  $\phi$  is the phase difference between the superconducting leads and  $I$  is the current through the junction. At zero bias current, the system is contained in a local potential well of depth  $2E_J$ . In this state, the change in phase  $\frac{d\phi}{dt}$  averages to zero and no voltage is seen. As the bias current is increased, the potential becomes tilted and the barrier of the well is lowered. When the critical current  $I_C$  is reached, the washboard potential is tilted to the point where local minimum becomes an inflection point and the system is no longer stationary but continuously changes its phase with time. At this point, the system switches from the superconducting to the normal regime.

If  $Q < 0.85$  the junction is overdamped.(18) This means that when the system is excited above the potential barrier, the energy of the system is quickly dissipated and it immediately is caught in the next potential well. In an overdamped system (at vanishing temperature), no voltage is developed until the bias current exceeds the critical current. Above the critical current the voltage smoothly evolves from  $V = 0$  to the ohmic regime  $V = IR$  as  $V = R\sqrt{I^2 - I_C^2}$ .

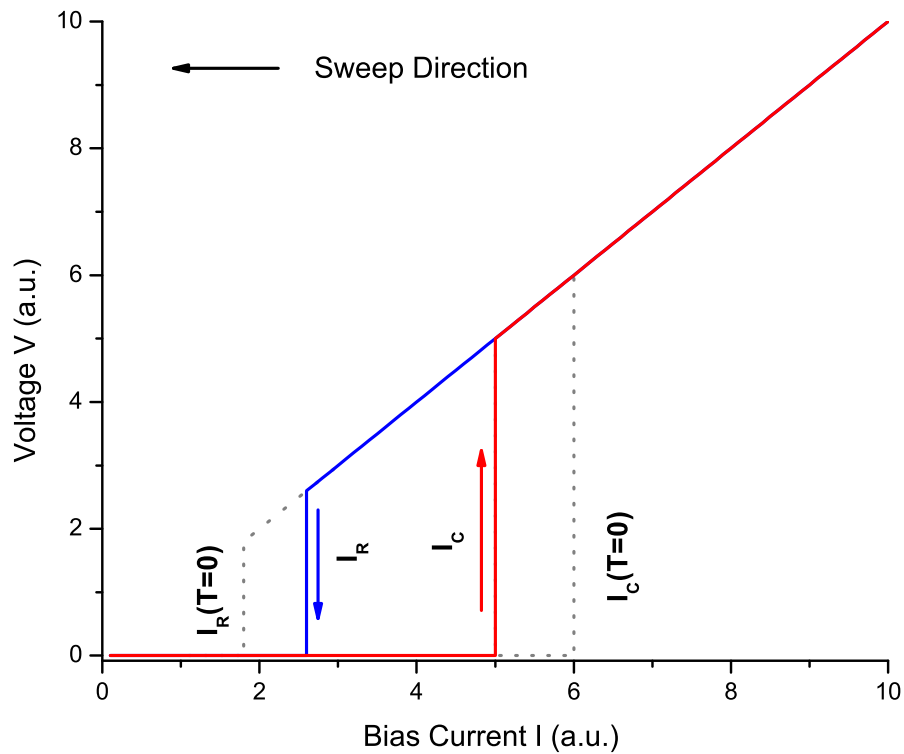


FIGURE 3.4: Shown here is a representation of a measurement of the current-voltage characteristic of an underdamped Josephson junction at non-zero temperatures. Initially, no bias current is applied and the junction is in the superconducting state. The bias current is then ramped up (red line), and at the point where the thermal noise is enough to excite the junction above its confinement potential the system switches to the normal state. The current at which this switch occurs is known as the switching current  $I_S$ . Now, the junction starts at high bias current and in the normal state. The bias current is then decreased (blue line). The junction will remain in the normal state until a retrapping current  $I_R$  is reached. The retrapping current  $I_R$  is lower than the switching current  $I_S$  because the energy provided by the bias current must be dissipated fast enough for the system to become trapped in one of the wells. At zero temperature the switching current is equal to the critical current  $I_S = I_C$ , and the retrapping current  $I_R$  is at its lowest value (gray line). As the temperature is increased the switching current is further suppressed but the retrapping current is enhanced.

However, if  $Q > 0.85$  then the junction is underdamped, meaning that any noise providing enough energy to excite the system above the potential barrier will cause the junction to switch to the normal state. At zero temperature this manifests in the abrupt switching of the voltage across the junction from  $V = 0$  to  $V = IR$  as soon as the critical current is reached. More over, when sweeping the bias current back down to switch the system into the superconducting state, the system will transition at a lower retrapping current  $I_R$ . As the system moves along the washboard potential, the energy provided by the bias current must be dissipated fast enough for the system to become trapped in one of the wells. In an underdamped junction, the dissipation is sufficient only for currents lower than the retrapping current  $I_R = 4I_C/\pi Q$ . When the temperature of the system is not equal to zero, the current at which the Josephson junction switches to the normal state  $I_S$  is further suppressed from the critical current and becomes statistically distributed from sweep to sweep, as the increased thermal noise at higher temperatures is capable of exiting the system above the potential well at lower and lower bias currents. The amount by which the switching current  $I_S$  is lowered compared to  $I_C$  can be determined by measuring the statistical distribution of the switching currents  $I_S(2)$ . However, for a case when a Josephson junction is in the Phase Diffusion regime, it is possible to extract the critical current  $I_C$  by measuring the junction zero-bias resistance(19; 20).

### 3.3 Phase Diffusion

We can examine a regime where at a given bias current the thermal noise is sufficiently large to excite the Josephson junction out the local minimum in the washboard potential, however, the damping is sufficient to retrap the system in the next local minimum of the potential. What is seen in this case is a system that constantly gets excited and then retrapped. Instead of the phase of the junction rapidly moving towards infinity, thus forcing the junction into it's normal state, the phase slowly but

constantly moves down along the washboard potential never deviating far above the potential(2). This phenomenon is known as Phase Diffusion and is usually associated with a small, but non-zero voltage measured across the junctions even though the bias current is still well below the critical current.

The current-voltage characteristics of a Josephson junction in the phase diffusion regime can be expressed in terms of modified Bessel functions of complex order as follows:  $I = I_C \text{Im}(\frac{I_{1-i\nu}(E_J/k_B T)}{I_{-i\nu}(E_J/k_B T)})$ (19; 20; 21; 22). In this expression  $\nu = (eV/\pi k_B T)(R_Q/Z)$  where  $V$  is the voltage across the junction and  $Z$  is the impedance associated with the junction. We can see that as we increase the voltage across the Josephson junction, the current rapidly increases, reaches a peak and then falls back down. This peak current that a junction can reach is in fact the switching current of the junction  $I_S$ . For very low temperatures  $I_S$  approaches  $I_C$ , however it falls dramatically once  $k_B T$  becomes the order of  $E_J$ .

A convenient feature of the Phase diffusion regime is that a measurement of zero bias resistance  $R_0$  versus temperature allows one to calculate the Josephson energy of the junction  $E_J$ , and therefore, to find the critical current of the junction (even at higher temperatures). Even if  $k_B T < E_J$  and a nearly zero current is sent through the Josephson junction, for high enough attempt frequency (the frequency at which the phase tries to escape the confinement potential, typically of the order of  $\omega_P$ ), there will be some events that excite the phase out of the local potential well and therefore cause a small but detectable resistance in the junction:  $R_0 \propto (\frac{1}{k_B T}) \exp(-2E_J/k_B T)$ . The above relationship between the zero bias resistance  $R_0$  and temperature is universal, regardless whether the junction is overdamped, or underdamped(19; 20; 21; 22; 23). This has been previously observed in SIS Josephson junctions(24; 26; 25). However, the proportionality factor is different depending on whether or not a junction is over or under damped.

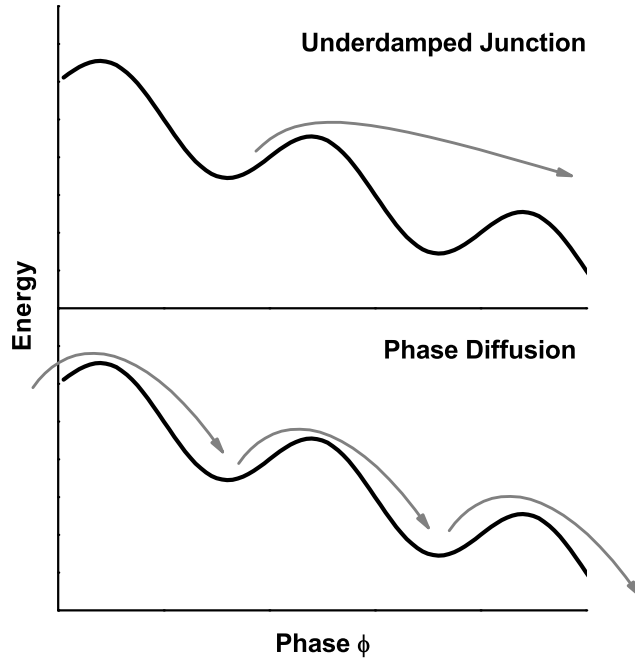


FIGURE 3.5: Conceptual schematic demonstrating the difference between a conventional underdamped junction and an underdamped junction in the phase diffusion regime. In both cases, the phase is confined to a washboard potential as described by the RCSJ model. In addition, in both cases the bias current flowing through the junctions is sufficiently high that the thermal noise in the junction can excite the system above the local confinement of the washboard potential. When excited above the confinement potential, conventional underdamped junction can not dissipate the energy fast enough to decay into another local minimum in the washboard potential. (Upper graph) The system gains energy, and the phase  $\phi$  travels unhindered to infinity, thus the superconducting state is destroyed. The phase diffusion regime, however, is different. (Lower graph) When the system is excited out of the local minimum in the washboard potential, the junction has enough damping to dissipate the energy and trap the system in the next potential well. However, once trapped, the system may once again be thermally excited above confinement, only to be trapped again. As a result, the phase of the system slowly travels along the washboard potential. Large amounts of energy are not gained and therefore the superconducting state is not destroyed, but unlike they system at zero bias, the phase of the system increases with time. A voltage  $V = \frac{d\phi}{dt}$  is developed across the junction. This voltage is much less than that developed across the junction in a normal state, and is proportional to the rate at which the system is thermally excited out of local confinement.

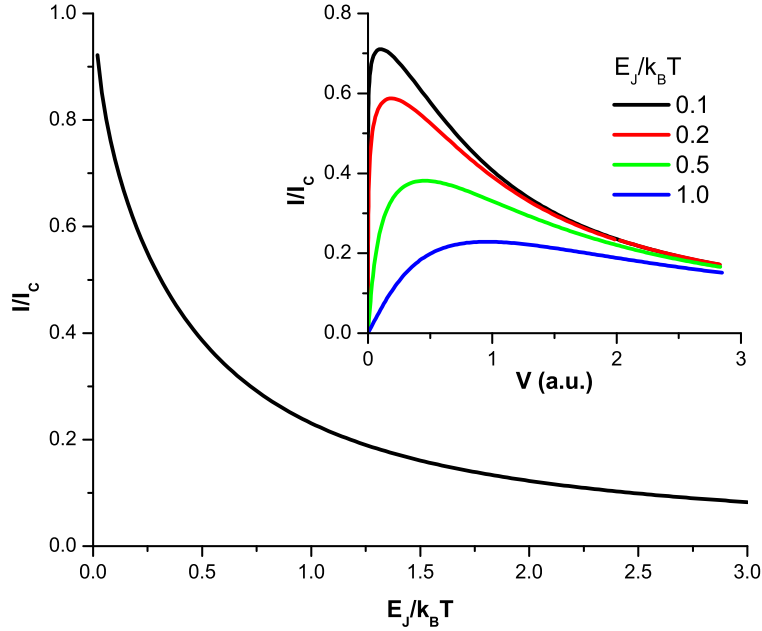


FIGURE 3.6: The inset shows the relationship between the current-voltage characteristic of the Josephson junction in the phase diffusion regime and temperature. The current through the junction is related to the voltage across the junction as:  $I = I_C \text{Im} \left( \frac{I_{1-i\nu}(E_J/k_B T)}{I_{-i\nu}(E_J/k_B T)} \right)$  with  $\nu = (eV/\pi k_B T)(R_Q/Z)$  where  $V$  is the voltage across the junction and  $Z$  is the impedance associated with the junction. One can see that as temperature increases or  $k_B T/E_J$  decreases, a higher value of voltage can be measured in the phase diffusion regime. More so, the maximum current that the junction can sustain is always less than the critical current  $I_C$  and decreases with increasing temperature. The extracted the maximum current through a junction  $I_S$  versus temperature is shown in the body of the graph. At  $T = 0$  the switching current approaches the critical current. However, the critical current is highly suppressed at higher temperature, and when  $E_J = k_B T$  the maximum current a junction can support in the superconducting state is reduced by more than  $2/3$ .

In case of an overdamped junction  $R_0 = RE_J \left( \frac{1}{k_B T} \right) \exp(-2E_J/k_B T)$  where  $R$  is the shunting resistance of the junction(23). If the junction is underdamped then  $R_0 = \frac{\hbar}{e^2} \hbar \omega_P \left( \frac{1}{k_B T} \right) \exp(-2E_J/k_B T)$ (21).

However, there also exists a second relationship of a special case of underdamped junctions. It is possible that a junction that is underdamped at DC becomes over-

damped at frequencies of order  $\omega_P$ . That is at very high frequencies the environment around the junction acts as a shunt across the junction. The associated shunting impedance is typically the impedance of free space  $Z_0 \sim 300\Omega$ . When the phase of the system is thermally excited out of the local potential well, the damping at the plasma frequency is more important as it is associated with the speed of the motion of the phase along the washboard potential. In this special case where an underdamped junction becomes overdamped at high frequencies (order of the plasma frequency)  $R_0 = 2\pi Z_0 E_J (\frac{1}{k_B T}) \exp(-2E_J/k_b T)$ (22).

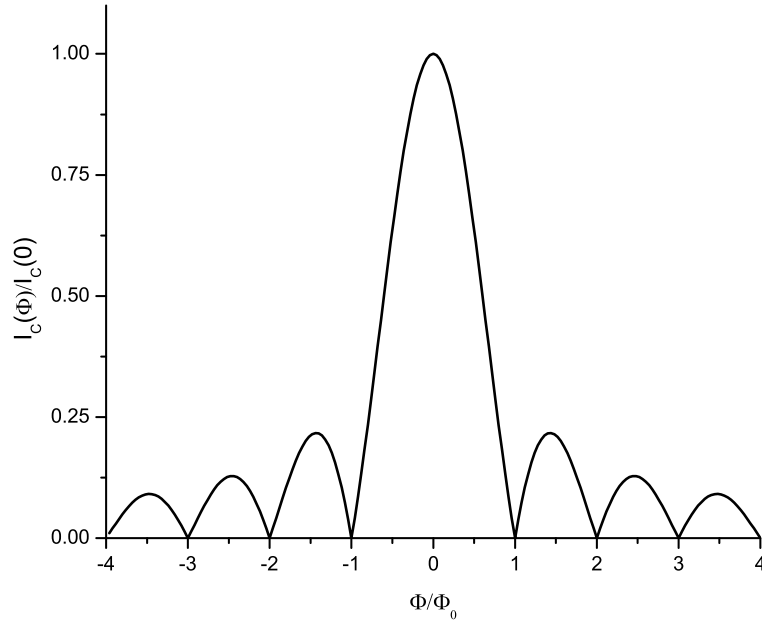


FIGURE 3.7: The critical current versus the magnetic flux sent through a Josephson junction. A magnetic flux causes current to flow along the width of the junction, which in turn linearly evolves the phase  $\phi(x) = 2\pi\Phi/\Phi_0 x/L$ . ( $L$  is the total width of the junction.) The local critical current through a Josephson junction is  $I(x) = I_C \sin(\phi(x))$ , and the total current through a junction is the integral of the local current along the junction width. Thus  $I = I_C \sin(\pi\Phi/\Phi_0)/(\pi\Phi/\Phi_0)$ . This result is known as the Fraunhofer pattern and is identical to that of light diffracting through a single slit.

### 3.4 Effects of Magnetic field

If a magnetic field is applied through a Josephson junction, a phase shift is created in the superconducting leads along the width of the junction. The change in phase of the superconducting state is described as  $\frac{d\phi}{dx} = 2\pi\Phi/\Phi_0 L$  where  $x$  is the position along the width of Junction,  $\Phi$  is the magnetic flux through the junction, and  $\Phi_0$  is the flux quantum. This means that the phase changes linearly along the width  $x$  of the junction. In turn, the critical current at a point along the width of the junction is  $I(x) = I_C \sin(\phi(x) - \phi_0)$ . Here  $\phi_0$  is the total relative shift of the phase, the value of which may change freely in order to maximize the total current through the Josephson junction. (This becomes relevant in non-ideal Josephson junctions.) The total current across the junction is the integral of all the individual currents which is equal to  $I = I_C \sin(\pi\Phi/\Phi_0)/(\pi\Phi/\Phi_0)(2)$ . The resulting current versus magnetic field relationship looks identical to the Fraunhofer interference pattern. The number of visible oscillations are usually taken as a measure of the quality of the Josephson junction.

### 3.5 SNS

A Josephson junction can be made by replacing the insulating material between two superconductors with a normal metal. These devices are typically called Superconductor-Normal metal-Superconductor (SNS) Josephson junctions. Unlike regular junctions where the insulator is only a few nm thick, SNS Josephson junction can have normal metal sections that are several  $\mu m$  in lengths. These junctions exist due to the proximity effect, where the Cooperpairs inside a superconductor penetrate some distance into the normal metal(2).

At vanishing temperature  $T = 0$ , the critical current in a traditional SIS Josephson junction is related to the superconducting gap  $\Delta$  as:  $eR_N I_C = \frac{\pi}{2}\Delta(27)$ . ( $R_N$  is

the normal resistance of the junction.) This is also the case for short SNS Josephson junctions operating in the ballistic regime. However, it has been found that for the case of diffusive SNS Josephson junctions, the superconducting gap  $\Delta$  is no longer the relevant parameter. Instead, the current through the junction is related to the Thouless energy  $E_{Th}$  as:  $eR_N I_C = 10.82 E_{Th}$  (28). The Thouless energy  $E_{Th} = \hbar D/L^2$  is the characteristic energy scale in diffusive conductors and is related to the diffusion constant of the metal  $D$  scaled by the size of the system  $L$ .

At temperatures close to the superconducting transition temperature  $T_C$  the critical current through a SNS Josephson junction is further suppressed as the cooper-pair concentration inside a normal metal decays exponentially with distance away from the contact to the superconductor. The maximum current through an SNS junction is therefore limited by the exponentially suppressed critical current in the middle of the normal metal section:  $I \propto \exp(-L/L_T)$ . Here,  $L$  is the length of the normal



FIGURE 3.8: Schematic representation of a lateral Superconductor-Normal Metal-Superconductor (SNS) Josephson junction. The schematic is a cut along the vertical axis of a conventional metal SNS Josephson junction design. Two superconducting metal leads are separated by a metal layer. The length of this layer can be as long as several  $100nm$  while still maintaining a supercurrent. The supercurrent through an SNS junction can exist due to the proximity effect, where the Cooperpairs inside a superconductor penetrate some distance into the normal metal. At  $T = 0$  the critical current of such a junction falls with the junction length  $L$  as  $I_C \propto \frac{D}{L^2}$ . Where  $D$  is the diffusion constant of the metal. For higher temperatures (close to  $T_C$ ), the Cooper-pair concentration inside a normal metal further decays exponentially with distance away from the contact to the superconductor. Therefore, critical current is further suppressed as:  $I \propto \exp(-L/L_T)$ . Where  $L_T = \sqrt{\hbar D/2\pi k_B T}$  is the characteristic thermal length.

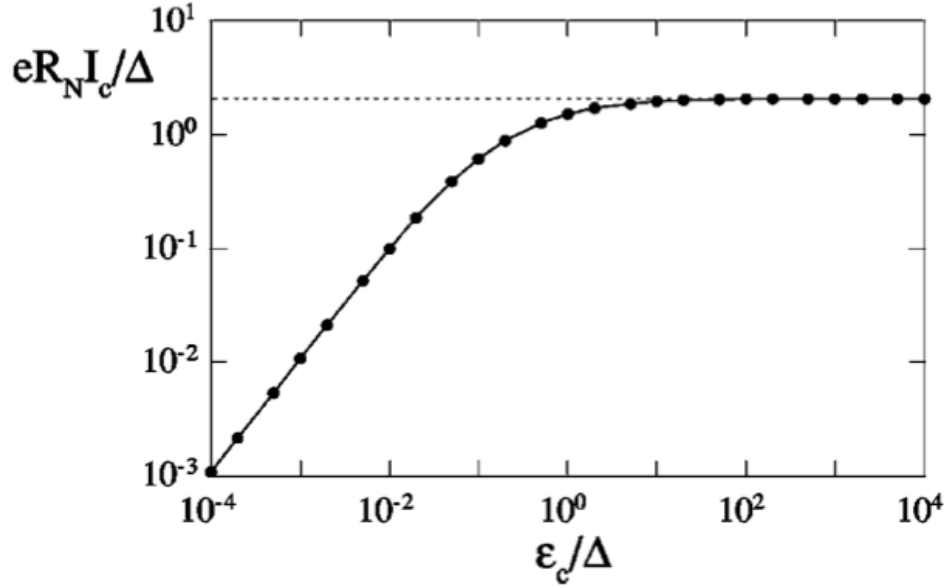


FIGURE 3.9: The relationship between the critical current, Thouless energy, and the superconducting gap. It has been numerically calculated that at zero temperature the critical current through an SNS Josephson junction depends on the Thouless energy  $E_{Th}$ .  $eR_N I_C = 10.82E_{Th}$ . (The variable  $R_N$  is the normal resistance of the junction.) However, this relationship holds only for long SNS junctions, meaning that the Thouless energy is less than the superconducting gap  $E_{Th} < \Delta$ . When  $E_{Th} > \Delta$ , the SNS Josephson junction is ballistic, meaning that the electrons do not scatter as they travel through the normal metal section and the critical current now depends on  $\Delta$ .

metal section and  $L_T = \sqrt{\hbar D / 2\pi k_B T}$  is the characteristic thermal length(28; 29).

The behavior of the SNS Josephson junctions at "medium" temperatures  $E_{Th} < T < T_C$  has been numerically analyzed as shown in Figure 3.10. In addition for a temperature range  $T > 5E_{Th}$  the critical current through an SNS Josephson junction dependence on temperature and the coefficient of diffusion can be expressed analytically as:  $eR_N I_C = \frac{32}{3+2\sqrt{2}} E_{Th} (\frac{L}{L_T})^3 \exp(-L/L_T)$ (28).

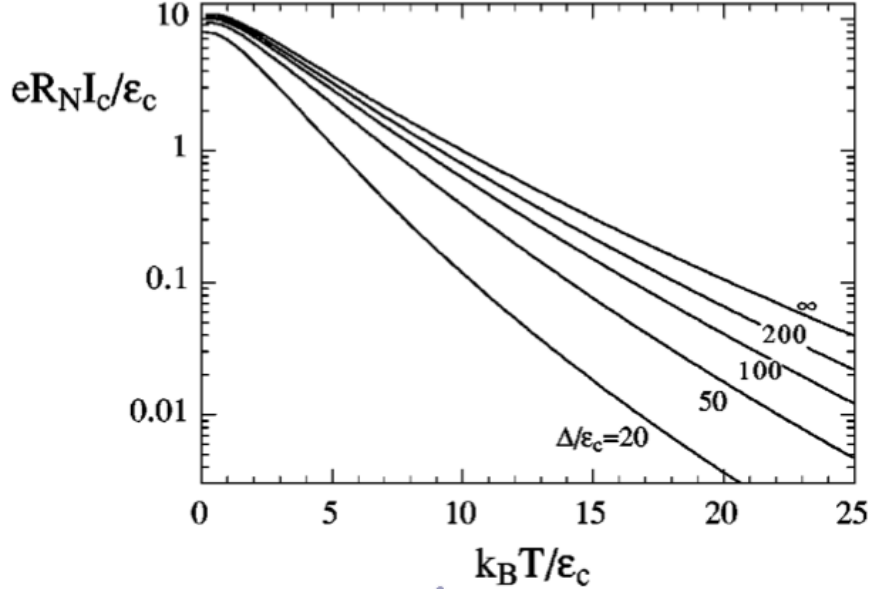


FIGURE 3.10: Plotted here is the critical current dependence on temperature in an SNS Josephson junction. As the temperature of an SNS Josephson junction is increased, the critical current through the junction is exponentially suppressed with the thermal length  $L_T = \sqrt{\hbar D / 2\pi k_B T}$ . This relationship can be described analytically in the high temperature regime  $T > 5E_{Th}$ . Then, the critical current is:  $eR_N I_C \propto E_{Th} (\frac{L}{L_T})^3 \exp(-L/L_T)$ . ( $R_N$  is the normal resistance of the junction,  $L$  is the total length of the normal metal section and  $E_{Th}$  is the Thouless energy.)

### 3.6 Graphene based SNS Josephson junctions

SNS Josephson junction devices that utilize graphene as the normal metal section have attracted some attention. Typically, a graphene crystal is contacted by aluminum superconducting leads with a thin titanium contact layer in order to reduce the contact resistance. Such devices require the use of dilution refrigerators in order to achieve temperatures at which a supercurrent through graphene is observed. It has been found that the critical current  $I_C$  through a graphene based SNS Josephson junction depends on the gate voltage applied to the graphene.(30; 31) The critical current is smallest at the Dirac point of graphene, and increases smoothly as the gate is shifted in either direction away from the Dirac point.

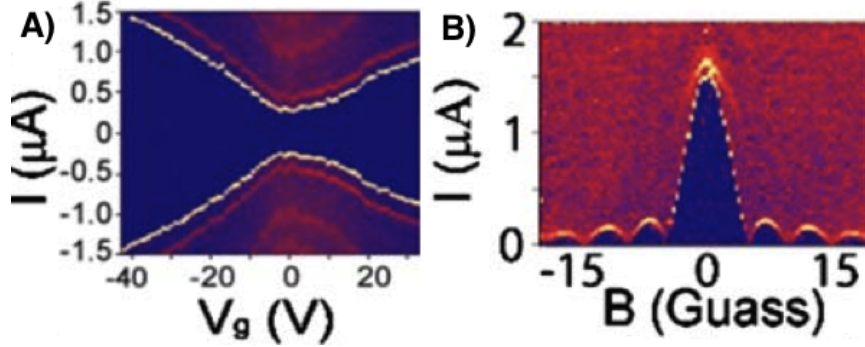


FIGURE 3.11: Figure A shows a map of voltage across a graphene based SNS Josephson junction versus the bias current and the gate voltage. A uniform blue region of the map signifies a zero measured voltage across the junction meaning that the junction is in the superconducting regime. For each gate voltage the region of the bias current where zero voltage is measured is bound by the critical current  $I_C$ . We can see that the critical current through a graphene based junction is lowest at the Dirac point  $V_{gate} = 0$  and increases as the system moves further and further away in gate voltage. Figure B shows a map of voltage across a graphene based SNS Josephson junction versus the bias current and magnetic field applied perpendicular to the graphene crystal. It can be seen that the critical current dependence on magnetic field, follows the classical Fraunhofer pattern dependence.

The magnetic field modulation of the critical current has been measured in graphene and was found to reproduce the classical interference result(30).

Finally, a hysteresis between the switching current  $I_S$  and the retrapping current  $I_R$  has been observed in graphene based junctions. However, it has been concluded that this hysteresis is caused by overheating of the device, not due to the junction being underdamped(32). When the Josephson junction is in the superconducting state, no power is dissipated in the junction. However, when critical current is reached, the junction switches to a resistive state and the temperature locally rises. Even as the bias current is reduces, enough power is delivered to the junction so that the temperature of the junction suppresses the switching current. The Josephson junction transitions back into the superconducting state only once the bias current becomes small enough that switching current of the junction at the increased junction

temperature is equal to the bias current.

By switching the superconducting material from aluminum to lead, it is possible to achieve a supercurrent through a graphene based SNS junction at much higher temperatures. This reduces the heating effects in the junction due to a higher junction Josephson energy  $E_J$  and better heat conductivity at higher temperatures.

## Sample Preparation

This chapter will cover the details of creating a Superconductor-Normal metal-Superconductor Josephson Junction. The junction utilizes graphene as the normal metal section and lead (Pb) as the superconducting contacts.

### 4.1 Graphene Deposition

The most common way of depositing graphene on a silicone (Si) substrate is known as mechanical exfoliation(7). In it's basic form, the method uses common household Scotch brand tape to peel a thin, flat layer of graphite from a source flake, typically a block of HOPG (Highly Oriented Pyrolytic Graphite). (Cleaner processes use Nitto tape instead of household tape.) The tape, with the now attached layer of graphite is then rubbed over a cleaned Si substrate. This rubbing action will leave few layer thin flakes of graphite on the surface of the SI wafer. Some of these flakes would only be a single atomic layer thick, hence: graphene. One of the problems with this method is that a large amount of charged impurities is left on the substrate. Left alone, these impurities locally gate the graphene flake. As a result, the Dirac cone structure is widened or completely destroyed, and the Dirac point is shifted far in

voltage from zero gate. In order to clean the graphene from these charged impurities, the sample is annealed at high temperatures. Unfortunately, because we use lead (Pb) as the leads connected to the graphene, we are unable to anneal our samples without melting and damaging the metal contacts. We have slightly modified the traditional exfoliation method in order to minimize dirt on our samples.

Most graphene flakes were made from natural graphite flakes instead of HOPG graphite, as it was believed that natural graphite crystals have cleaner layers. However, the later graphene samples were successfully obtained by using ultra high quality HOPG graphite. We use dicing saw tape (Nitto) as it does not leave a residue when it contacts the substrate but is strong enough to peel the graphite layers from the bulk crystal. Nitto tape is adhered to two glass slides in order to create a hard and flat, but sticky surface. A graphite flake is placed between two glass slides. The two pieces of glass are then separated and the graphite flake is split into two pieces. During this process some of the clean inner sheets of graphite peel off the bulk graphite flake and lie on the bulk surface easily accessible by fine point tweezers. We select the most clean, thin, and flat of those flakes to transfer to a silicone wafer chip.

Our substrate features a  $280nm$  oxide layer, which is the optimal length for Fresnel interference effects to maximize the contrast between the graphene flake and the background (33). Every single silicone chip as well as all of our metal tools are RCA cleaned prior to receiving or handling graphene. We use a fine point metal pick and fine point tweezers to pick up the loose graphite flake from the glass slide without touching the tape. This flake is placed on the substrate and is manipulated to lay flat on the surface. (If the substrate and the graphite are clean, the flake will adhere well to the surface. If the process is dirty, there will be no adhesion of the graphite to the substrate.) We then use the metal pick to rub the graphite over the entire surface of the chip. During this process the flake will tear apart into smaller pieces. The emphasis of this process is to have the flake tear apart naturally as opposed to



FIGURE 4.1: An optical image of a single atomic layer graphene flake. The graphene is a faint triangular shape in the middle of an image. It is about  $30\mu m$  long with a base of  $10\mu m$ . The large, irregular shape to the side of the graphene is a piece of multi-layered graphite. The fainter, more transparent edges of that shape indicate that the number of crystalline layers decreases at the edge for that particular flake. The majority of the carbon material deposited using the exfoliation method is in form of large, many-layer graphite flakes, and during the lithographic process care must be taken to avoid crossing this graphite when routing the metal leads. Finally, the regular, patterned shapes in the image is the lithographically defined metal search pattern. This pattern locates the graphene flake relative to the rest of the chip and is required to route the contacts to the graphene.

creating cutting trenches with the metal tool. We then visually inspect the sample for the presence of graphene. If no graphene is found, the multi-layer graphite pieces on the surface can be further exfoliated by applying and peeling off fresh dicing saw tape (Nitto) directly to the substrate surface.

When using this process, the tape never comes in direct contact with any material

that would later become a part of the sample, and the dicing saw tape (Nitto) does not leave a residue. This results in a relatively clean sample. The Dirac point of our graphene samples would typically be shifted by around  $40V$  in gate, however, the Dirac cone structure remained preserved.

## 4.2 Graphene Characterization

The number of atomic layers in a graphene flake determines its color and transparency. A single layer can be identified just by a trained eye. It is also possible to identify single layer flakes by looking at the color reading of a CCD detector(33; 34). However, in order to definitively determine the number of layers as well as make a statement about the quality of a given flake, characterization by Raman spectroscopy is needed. We analyze every graphene flake under Raman spectroscopy prior to doing any further processing.

The Raman spectrum of graphene features three peaks: D, G, and 2D(35). The height of the D peak in the spectrum is related to the number of lattice defects in the graphene sheet. The height of the G peak is proportional to the number of layers in a graphene flake, however, it is difficult to calibrate. Instead we look at the 2D peak, which is independent of height but instead varies in shape depending on the number of layers. For a single layer of graphene, the 2D peak is highly symmetric and has a shape of a Lorentzian. Multi-layer sheets of graphene have asymmetric 2D peaks which are a result of a summation of several shifted Lorentzians of varying height. (A two layer sheet of graphene would have four Lorentzian shapes contributing to the overall shape of the 2D peak.) Unlike the case for a single layer, the exact shape of the 2D peak of a multi-layer crystal depend on the imaging laser frequency(35).

We characterized the sample using the commercial spectrometer (Horiba Jobin Yvon LabRam ARAMIS). The laser light frequency was selected to be  $633nm$ . The size of the aperture was not an issue, as the focused beam of  $\sim 25\mu m$  in diameter

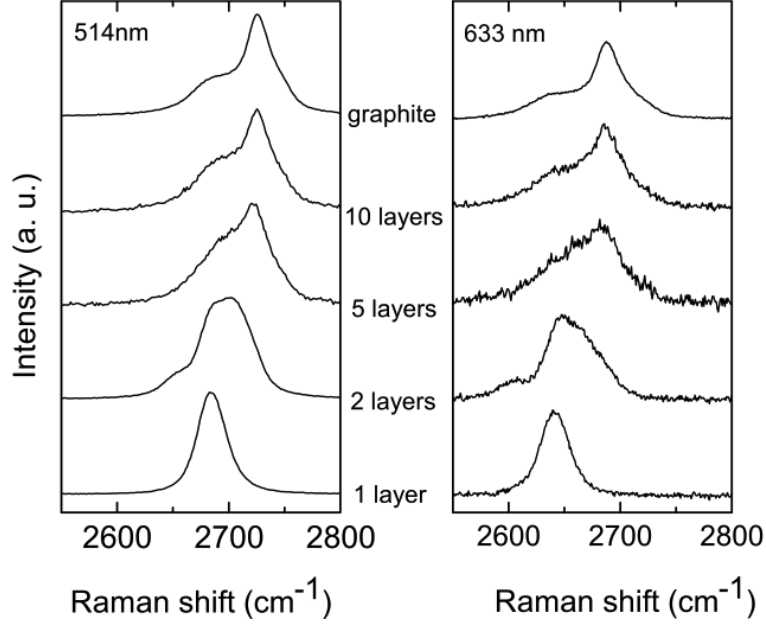


FIGURE 4.2: Evolution of the 2D peak in the the Raman spectrum of graphene(35). The 2D peak for single layer sheet of graphene should fit well to a single Lorentzian shape, and therefore, should have very good symmetry. Multi-layer sheets of graphene feature a 2D peak that has a shape of a summation of several Lorentzians each of varying height and slightly shifted fro  $2690\text{cm}^{-1}$ , and would have an asymmetric shape. A two layer crystal would have a 2D peak that fits well to a sum of four Lorentzians(35). The exact shape of the 2D peak for a multi-layer sheet of graphene depends on the probing beam frequency. Presented here are maps for 2D peaks excited by a  $514\text{nm}$  and a  $633\text{nm}$  laser. For the case of the samples used in our measurement, only single layer samples were needed.

was sufficient to isolate the contribution of the studied flake. We set the grating, to  $1800\text{gr}/\text{mm}$  which gave us a measurement range of  $0 - 4000\text{cm}^{-1}$  (this was the highest resolution available to us). The resulting spectrum included the contribution of the substrate, but all those features present were below  $1200\text{cm}^{-1}$  which are below the first graphene peak (D). With our flakes, we observe a small D peak at about  $1380\text{cm}^{-1}$ , a G peak at  $1590\text{cm}^{-1}$  that is much smaller than the 2D peak at  $2690\text{cm}^{-1}$ . We visually, inspect the 2D peak for symmetry in addition to fitting the peak to a Lorentzian function. A good fit to a Lorentzian allows us to conclude that the chosen graphene flake is indeed a single layer sheet.

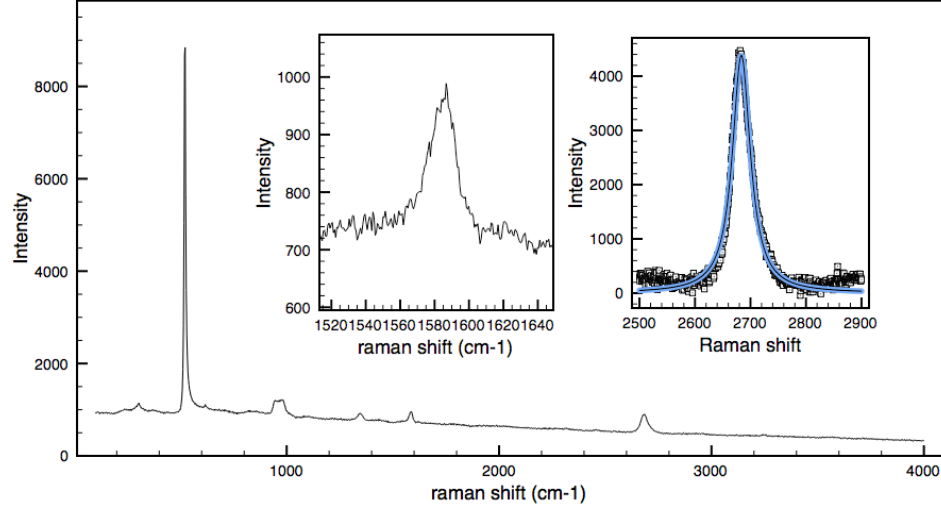


FIGURE 4.3: Raman spectrum of our typical graphene sample. Main graph: Full spectrum which includes the features attributed to the silicone substrate. The large  $500\text{cm}^{-1}$  peak is due to the silicon-oxide layer. We observe three peaks related to graphene: a D peak at  $1380\text{cm}^{-1}$ , a G peak at  $1590\text{cm}^{-1}$ , and a 2D peak at  $2690\text{cm}^{-1}$ . The D peak is related to the number of defects in the graphene crystal lattice. In the majority of our sample the D peak is barely discernible or is lost in the noise, but for the purpose of demonstration a higher defect sample was chosen. Left Insert: The G peak of graphene. The height of the G peak scales with the number of atomic layers in our measured crystal. However, this measurement requires extensive and frequent calibration as the background of the measurement system varies with time. Right Insert: The 2D peak of graphene with a Lorentzian fit. The quality of the fit to a single Lorentzian shape and the visual symmetry of the peak of this particular measurement suggest that the sample is a single layer of Graphene.

### 4.3 Lithography

We used electron beam lithography to define a pattern for all the metal contacts required on the sample. The lithography was done using an EFI XL30 scanning electron microscope fitted with NPGS lithography software. Every sample underwent three lithographic stages: search pattern, bonding pads/large leads, lead (Pb) contacts to graphene. Both the search pattern and the pads/ large leads stages were defined by the standard lithographic recipe using A4 495 weight PMMA as the electron beam

resist. Dichloromethane (DCM) was used as the liftoff chemical instead of the more commonly used Acetone as it is much cleaner and less damaging to graphene. We deposited a 10/20nm bilayer of Cr/Au to create both the search pattern and the bonding pads. The later samples were designed to extend the Cr/Au leads as close to the graphene as possible in order to minimize the amount of superconducting material. This was done in order to minimize the parasitic capacitive coupling between the superconducting leads which was dominated by the lead-substrate-lead capacitance across the, 300nm oxide layer. The Pb contact stage of the lithography was done with a slightly different recipe. We typically deposited 100 – 120nm of Pb which meant that the electron beam resist had to be thicker. As a result, we deposited two layers of resist: either two identical layers of A4 weight 495 PMMA, or, in order to create a better defined undercut, a bilayer of A8 weight 495 and C2 weight 950 PMMA. Our method of Pb deposition requires a slight undercut in the exposed resist, therefore, the exposure dose has to be calibrated prior to making a batch of samples.

#### 4.4 Lead Deposition

We developed a method of depositing thin lead (Pb) leads of small height. Thin leads are required in order to minimize the parasitic capacitance between the superconducting sections and to maximize the available area of the graphene contacting the lead. Leads of small cross section are needed in order to maximize the current density along the Pb contacts, as discussed later. Under typical conditions, thermally evaporated lead (Pb) would form grains that are more than 300nm wide and will not form a uniform film less than 200nm thick. We were able to deposit uniform Pb film strip as thin as 300nm and a height of less than 30nm. (However, a superconducting Pb film needed to have a height of at least 40nm.) First of all, palladium (Pd) was used as a sticking layer between the graphene flake and the lead (Pb) as it is known

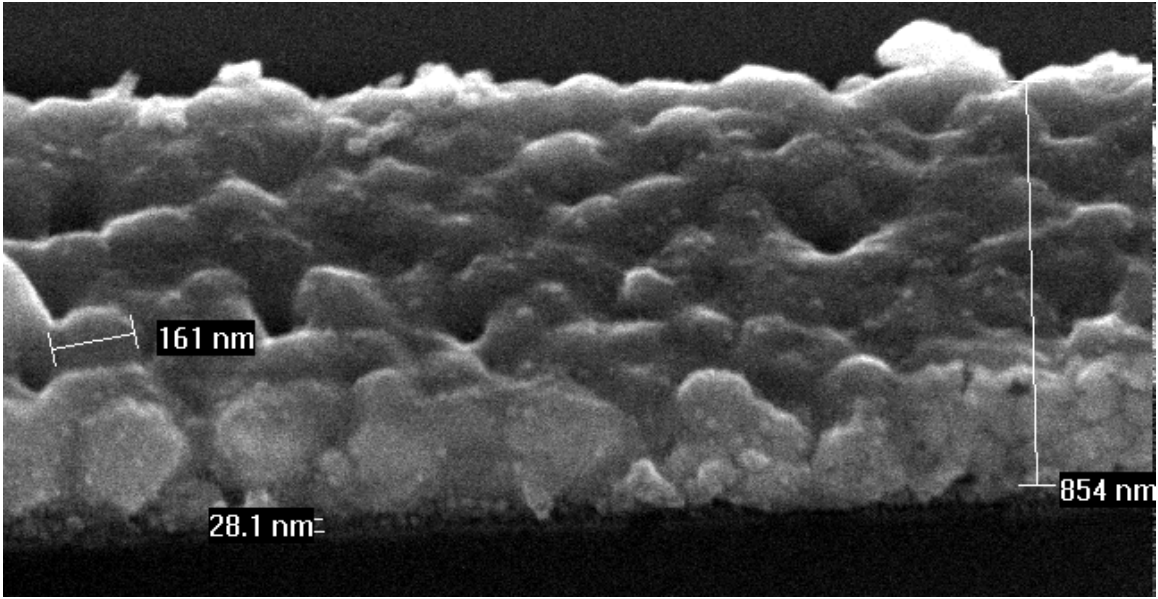


FIGURE 4.4: Scanning Electron Microscope (SEM) image showing the structure of the superconducting electrodes. The image taken is that of a calibration sample, meaning, no graphene is present. The sample is tilted 45 degrees with respect to the imaging electron beam in order to better show the bi-layer structure. The portion of the superconducting leads that contacts the graphene are typically  $1\mu m$  in width and about  $10\mu m$  long. They are made from a Pd/Pb metal bi-layer, where the lead (Pb) acts as the superconducting metal, while the palladium (Pd) is used in order to form an electrically transparent contact to the graphene. The Palladium layer is only 2 – 4 nm thick so as to have minimal effect on the superconducting proximity effect between the lead and the graphene. However, it is important that lead does not touch the graphene directly, and therefore the palladium layer must stick out somewhat past the lead layer of the electrode. For this particular sample the Pd sticks out 25 – 30 nm beyond the Pb portion. This is achieved by properly calibrating the undercut of the e-beam resist during the lithographic process, and by continuously tilting the sample  $\pm 10$  degrees as Pd is being evaporated. For the majority of the samples, the lead (Pb) portion of the contacts is 80 – 120nm thick, and has a grain size of about 150nm. To achieve this grain size the lead was evaporated at a relatively high pressure  $2 * 10^{-5} mbar$  and deposition rate 1.5 – 2.0nm/sec. If smaller grain size and smaller metal thickness is required, the sample substrate must be chilled close to liquid nitrogen temperature during the evaporation process.

to create highly transparent electrical contact to graphene(36; 37). We deposited  $2 - 4nm$  thin films of Pd which is enough to form a continuous film, but thin enough to minimize it's negative effects on superconductivity. During deposition of Pd, the substrate was continuously tilted back and forth  $\pm 10$  degrees. This ensured that Pd covered the entire exposed area of the substrate, including the surface beneath the undercut that would normally remain metal-free. During deposition, lead (Pb) atoms tend to travel quite a bit, therefore under normal conditions it would flow past the palladium layer and directly contact the graphene. However, when this tilting technique is used, the palladium sticking layer extends  $10 - 40nm$  past the Pb layer. Prior to deposition we mechanically cleaned the Pb source from oxide by melting it with the soldering iron and moving the melted bead of lead around on a clean surface. The lead oxide adheres selectively to a soldering iron leaving the rest of the Pb source much cleaner and shinier. We evaporate lead at a relatively high chamber pressure of  $2 * 10^{-5}mbar$ . However, the chamber is first pumped down to at least  $7 * 10^{-7}mbar$  and then clean nitrogen gas was used to raise the pressure back up. The deposition rate of somewhere between  $1.5 - 2.0nm/sec$  is also fairly high. Both the high pressure and high rate of deposition are needed in order to have lead with small domain sizes. If contact height of less than  $80nm$  or width of less than  $300nm$  is needed, the substrate has to be cooled during deposition. We have outfitted our evaporation chamber with a liquid nitrogen trap and a cold finger that cools the silicon substrate to  $150K$ . The chilled substrate quickly cools the lead (Pb) particles as soon as they come in contact with the surface and prevents them from flowing, and congregating in domains.

After the deposition, care must be taken to ensure that the sample reaches room temperature prior to exposing it to the atmosphere. Any condensation of water on the substrate instantly oxidizes the thin lead film. In addition, the sample must be kept below  $70C$  or the lead will travel. Even with these precautions, the lifetime

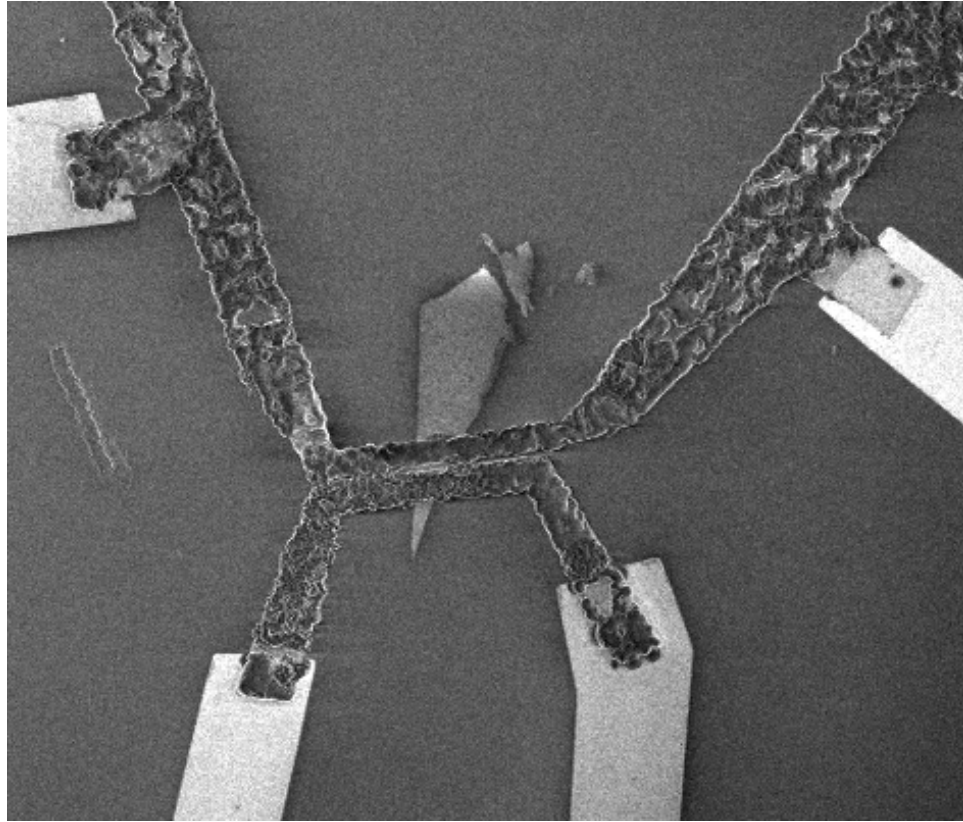


FIGURE 4.5: Scanning Electron Microscope (SEM) image of a Pb-graphene-Pb sample after measurement. The graphene is seen as a triangular shape in the middle of the image. Two Pd/Pb electrodes cross the graphene crystal thus creating a Superconductor-Normal metal-Superconductor Josephson junction. In this image, the lead contacts are highly distorted and appear to short the graphene crystal. In fact, what is seen, is oxidized lead. The thin lead electrodes degrade very quickly in the atmosphere, and will oxidize to the point where no superconducting features are seen within a week. In addition, heating the sample above  $70C$ , or exposing the sample to moisture will oxidize the lead within minutes. The sample shown here was measured in a "dipping probe" cryostat and became exposed to moisture after it was extracted from the liquid helium. Finally, the image shows bright, un-oxidized Cr/Au leads.

of the sample in atmosphere is at most several days. We typically store completed sample in vacuum or immediately install it into the measurement system. Room temperature resistance of the Pb-graphene-Pb junction in a freshly made sample is no more than  $\sim 300\Omega$  (for a shape where  $\frac{Width}{Length} \sim 10$ ). The longer the sample is exposed to the atmosphere, the higher this resistance will become, and supercurrent through the junction will not develop if the sample degrades to have resistance of more than  $\sim 1000\Omega$ .

## Measurement Setup

This chapter describes the measurement setup used to study the Superconductor-Normal metal-Superconductor Josephson Junction. It will cover the measurement electronics, filtering and shielding, and the cryostats used in the measurement.

### 5.1 Overview

We characterized our graphene-based Josephson junctions by measuring the junction conductance versus four parameters: bias current, gate voltage, temperature, and perpendicular magnetic field. The samples were measured by a pseudo 4-probe measurement, where the four individual probes converged into two on the superconducting lead (Pb) portion of the sample. While the Pb leads do not contribute to the measured resistance below their critical temperature, the resistance due to the graphene-metal interface is not canceled out(38).

We have set up the system to simultaneously make a direct DC measurement of the junction voltage versus bias current, as well as a lockin amplifier measurement of differential resistance. The lockin measurement allows for a much more precise measurement of the junction resistance, while the DC measurement can clearly show the

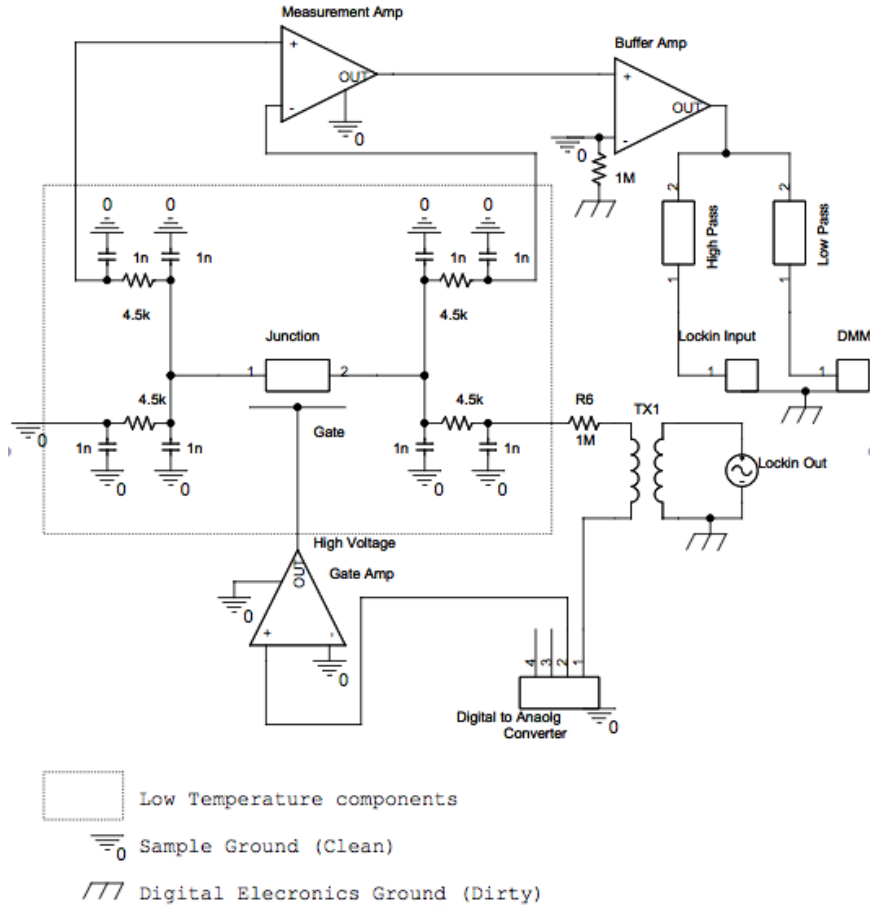


FIGURE 5.1: Presented here is a schematic description of a typical setup used to measure the graphene based SNS Josephson Junction. Enclosed by the dashed square is the portion of the setup that is located at cryogenic temperatures. Four leads (plus the gate) make contact to the sample after being passively filtered at the base temperature. Thus, the sample was measured by a pseudo 4-probe measurement where the four individual probes converged into two on the superconducting lead (Pb) portion of the sample. While the Pb leads do not contribute to the measured resistance below their critical temperature, the resistance due to the graphene-metal interface is not canceled out. Care was taken to eliminate ground loops and to avoid fluctuations in ground voltage due to digital electronics. Therefore, two grounds were defined: the clean sample and cryostat ground, and the dirty digital measurement electronics ground. The current through the sample was set by a 1M resistor, a voltage output from a DAC for DC bias, and the output from a lockin amplifier sent through a transformer for AC modulation. The voltage is measured by a fully analog differential amplifier which shares the ground with the sample, followed by a buffer amplifier which breaks the ground between the sample and the measurement. Gate voltage was applied by a high voltage amplifier which also broke the ground between the input and output signal so as to eliminate the ground loop caused by the shared ground between the different output channels of the DAC.

nature of discontinuous jumps associated with the Josephson junction transitioning between the normal and the superconducting states .

Extreme care was taken to create a low noise environment. The signals going to the sample are filtered and shielded at low temperatures with care being taken to eliminate both the low frequency and the RF frequency noise. The noise of our measurement electronics is calculated and devices are made such that the noise levels are below the scale of the features we are trying to measure. Finally, the ground connections of all of the measurement devices are carefully designed in order to break ground loops notorious for picking up  $60Hz$  noise as well as to separated the ground of the sample from the noisy ground of the digital measurement electronics(39).

Finally, thermal connections were designed to be robust as to eliminate, or at least reduce the local heating effects of the measurement current being sent through the sample. Care was taken, to make direct copper to copper connections of the signal leads where thermal connection was necessary. Bismuth was used as the soldering material in order to further improve thermal conductivity(40).

## 5.2 Room Temperature Electronics

In our measurement, all of the active electronic components were located at room temperature. Only the passive filters were cooled to the cryostat base temperature. The noise related to each piece of electronics that could send a signal directly to the measured sample was calculated for a bandwidth larger than allowed by our filter, and components were chosen such that their noise level would be small enough as not to destroy the relevant features we were measuring.

### 5.2.1 *Current Source*

Unlike conventional Superconductor-Insulator-Superconductor Josephson junctions, our SNS junctions have very low resistance even above their critical current (normal

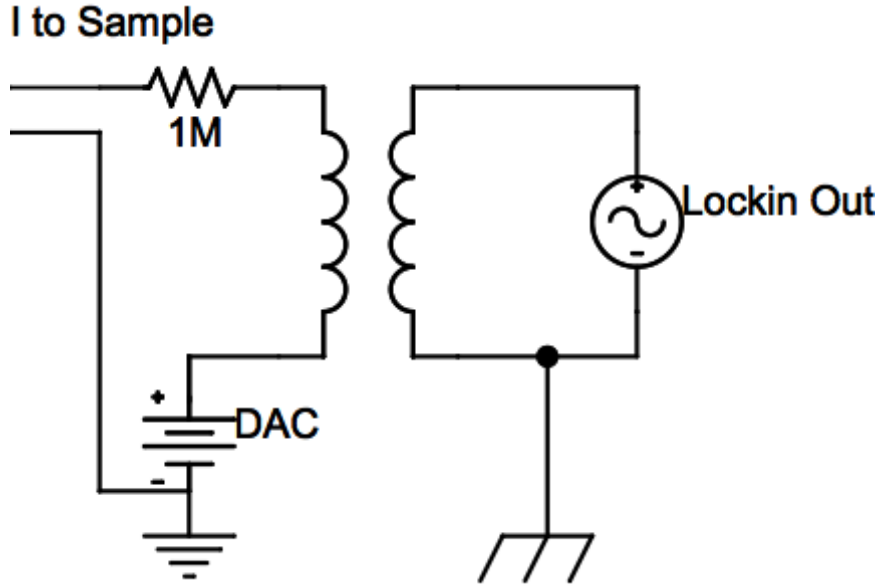


FIGURE 5.2: The total net resistance of the sample plus the filters that a bias current will encounter is no more than  $12k\Omega$ . In addition, the maximum current sent through the sample need not be above several  $\mu A$ . Therefore, a voltage applied to a  $1M$  resistor is sufficient to act as a current source. The DC current is set by the output voltage of the digital to analog converter which is optically isolated from the rest of the digital electronics and therefore sits on the clean cryostat ground. The AC current however, is taken from the output of the lockin, and is therefore isolated by the use of a transformer.

resistance  $R_n < 1K\Omega$ ). However the critical current across our samples remains on the order of  $I_C \sim 1\mu A$ , this means that a precision  $1M\Omega$  resistor is sufficient to act as a voltage to current converter. We require that the current sent to our sample contain both a DC and an AC component in order to perform lockin amplifier measurements, therefore we have designed our current source to passively add the AC and DC voltages. The AC voltage source was acquired from the sine generator output of the lockin amplifier through a transformer. By using a transformer, we break the ground connection between the output of our lockin. The DC voltage was sent directly from a digital to analog converter (DAC) and supplied to the lower leg of the transformer, thus adding current bias. We have separated the DAC from the

dirty digital ground by powering it with a floating power source and sending the digital signal through an opto-coupler.

### *5.2.2 Voltage Amplifier*

We have used three different differential amplifiers in order to measure voltage across our junction: a home made amplifier based on a commercial instrumental amplifier chip, a home made matched pair transistor-based amplifier, and a commercial pre-amp. In all three cases the amplifier had to be well grounded to the cryostat (that is it had to share the ground with the sample), and the amplifier had to be powered by a floating power source separate from all other active elements. However, this amplifier was followed by a second stage of amplification that also broke the ground between the cryostat and the measurement electronics.

Our first amplifier was based on an instrumental amplifier chip from Linear Technology (LT1167). We have chosen an instrumental amplifier instead of an operational amplifier because such a device does not utilize a direct feedback loop in order to set the gain, and therefore no current flows between the inputs and the outputs of the amplifier. An instrumental amplifier in its most basic form is a two stage amplifier consisting of an operational amplifier that is preceded by two followers (one for each input). The followers isolate the input signals from the output signals, while the operational amplifier handles the signal amplification. (The more advanced design of the instrumental amplifier chip that we used had the gain set in the first stage of amplification.) We chose the Linear Technology LT1167 chip due to its low voltage noise characteristics as well low power consumption since our device was powered by two 9-Volt batteries. The batteries were used to create a stable power source with very low ripple and to eliminate  $60Hz$  noise associated with typical power supplies. In addition, battery power created a floating device, meaning that our amplifier connected to only the ground of our measured device, thus eliminating ground loops.

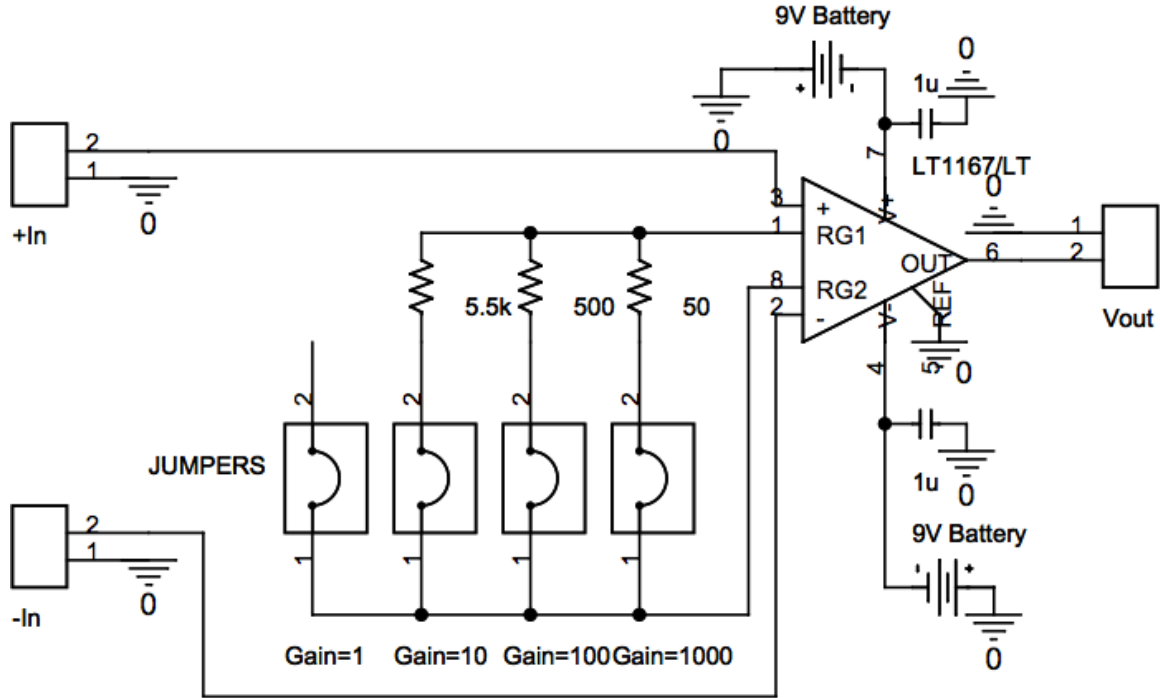


FIGURE 5.3: Schematic for differential amplifier used to measure the voltage across the SNS Josephson junction. This amplifier is based on the commercial LT1167 instrumental amplifier chip. The circuit is powered by two 9V batteries and accepts the ground of the input signal. The batteries create a low noise power source and eliminate ground loops that can be caused by sharing a power source between several devices. The ground is shared with the input signal as this setup is more efficient in shielding the un-amplified input from external noise. However, this setup requires a second stage of amplification in order to break the ground between the sample and the digital measurement electronics. Finally, this amplifier features selectable gain from 1 to 1000 by the use of jumpers.

Having our amplifier connected to the ground of our junction allowed for good shielding of the un-amplified voltage signal as well as anchored our amplifier relative to the Josephson junction, thus eliminating amplifier overload due to the ground of the junction and the ground of the amplifier accumulating large relative voltage. We have set the total gain of this amplifier to 1000 which resulted in the best signal to noise ratio for our device. The LT1167 amplifier has a high frequency noise rating of  $7.5 \frac{nV}{\sqrt{Hz}}$ , considering a bandwidth of  $1kHz$  (which is an order of magnitude larger

than allowed by the lockin input filters) we can set an upper limit of the total voltage noise to be  $0.24\mu V$ . The LT1167 chip has an input impedance of at least  $200G\Omega$  which, for a filter bandwidth of  $100kHz$  translates to a current noise of  $100fA$ . This noise is significantly less than our smallest AC current excitation sent by the lockin of  $10nA$ . However, the DC noise of the LT1167 amplifier is rated to be  $28\mu V_{p-p}$ , unfortunately this proved to be of the same order as the voltage created by the phase diffusion regime of our Josephson Junctions at the lowest temperatures as well as when the normal resistance of the junction was low.

In order to reduce the noise due to the voltage measurement electronics, we have designed a transistor based amplifier. We have utilized a Toshiba 2SK3320 JFET matched transistor pair as the first stage of signal amplification followed by a conventional amplifier chip in order to achieve higher gain as well as to isolate the transistors from any load that might be seen at the output of our amplifier. The JFET transistors feature only  $1.0dB$  or about  $1\frac{nV}{\sqrt{Hz}}$  of noise, in addition since the input signal only sees the gate input of the FET transistors, no current can flow from the amplifier back to the sample. Both the transistors and the second stage amplifier are low power devices and therefore, receive power through a set of voltage references resulting in a very stable power source. The working point of the transistors was set by three high precision ( $0.1\%$ ), low thermal drift ( $5\frac{ppm}{C}$ ) resistors, and chosen to have the the required voltage range while achieving the maximum gain of 15. The inputs of the transistors were tied to ground using  $1M\Omega$  resistors in order to prevent overload. The entire device was encased in an RF tight aluminum box. Unfortunately, the JFET matched pairs were designed to be only matched for AC signals, and resulted in a DC offset. Our attempts to compensate for this DC offset using the second stage of amplification were proved to be unstable, and therefore this amplifier was only used for measuring AC signal.

In our latest measurements (not presented in this work) we have chosen to use

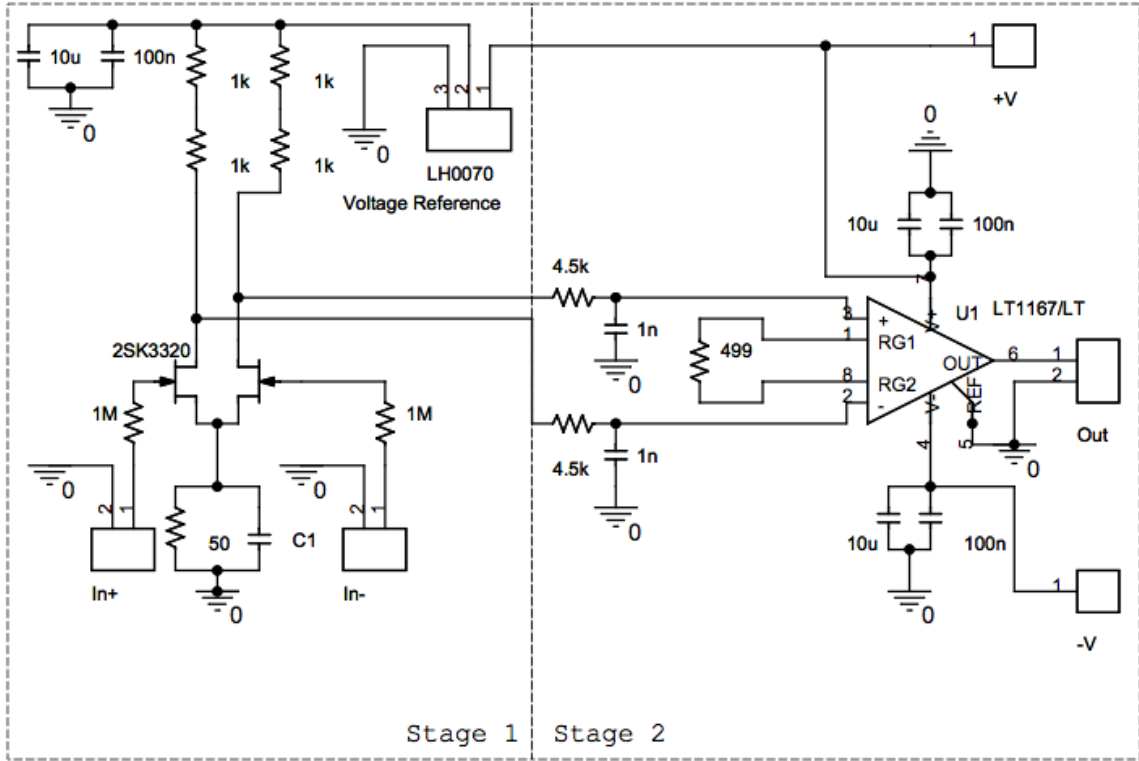


FIGURE 5.4: A two-stage, transistor based differential amplifier used to measure the voltage across the SNS Josephson junction. The initial stage of amplification is based on the Toshiba 2SK3320 J-FET matched pair. This transistor was chosen for its very low noise and low offset current characteristics. Due to the low power consumption of these transistors, a steady voltage signal can be provided by a 10V voltage reference. The working point of the transistors is set by 0.1%, low thermal drift  $5 \frac{ppm}{^\circ C}$  resistors, and chosen to have the the required voltage range of  $V$  while achieving the maximum gain of 15. The inputs of the transistors were tied to ground using  $1M\Omega$  resistors in order to prevent overload. The second stage adds additional amplification, an buffers the transistors from the load of the further measurement electronics. The entire device is enclosed in a milled, RF tight aluminum box separated into two sections, one for each stage.

a commercially available preamplifier to measure the voltage across the sample. We used the NF Corporation model LI-75A differential preamplifier, as it features only  $2 \frac{nV}{\sqrt{Hz}}$  of voltage noise. The input impedance of this amplifier is  $100M\Omega$ , which for a bandwidth of  $100kHz$  gives a current noise of  $4pA$ . We required a much smaller current for our samples, therefore, our supply current was created by an  $11M\Omega$

resistor (instead of  $1M\Omega$ ). In this setup, the  $4pA$  of current noise was still less than a one bit step of our DAC ( $30pA$ ). Unlike the previous amplifiers, the NF LI-75A was not battery powered, therefore, a ground breaker had to be installed on it's power supply in order to eliminate a ground loop.



FIGURE 5.5: A reference photo of the commercial pre-amplifier used to measure the voltage across our SNS Josephson junctions. The amplifier chosen is the NF corporation LI-75A differential preamplifier which features a gain of 100 and only  $2 \frac{nV}{\sqrt{Hz}}$  of voltage noise. This amplifier, also accepts the ground of the measured sample. Unlike the previous, custom made amplifiers, this commercial pre-amp is powered by a linear power supply which in addition shares the ground with digital electronics. Therefore, a ground breaker had to be installed in order to eliminate a ground loop.

### 5.2.3 Gate

The resistance of the graphene in our sample was altered by applying a gate voltage. This voltage was applied to the silicon substrate which acted as the back gate since it is isolated from the rest of the sample by  $300nm$  thick silicon oxide layer. In order to see dramatic changes in graphene resistance (as well as critical current), a gate voltage sweep close to  $\pm 50V$  is needed. As such, we utilized a home made high voltage amplifier. The gate amplifier was based on the Texas Instruments OPA445 operational amplifier which was chosen for its low noise characteristics as well as the ability to be powered by up to  $\pm 45V$ . We designed the gate amplifier as a

two stage, three channel summing amp. The first stage of our amplifier consisted of three instrumental, differential input, follower amplifiers (one for each input channel). The goal of the first stage is to break the ground between the input voltage and the amplifier ground. The second stage of amplification was the OPA445 op-amp set up as a summing amplifier. We designed one input channel to have a gain of 5 in order to achieve the maximum voltage swing from the  $\pm 10V$  signal from the DAC. A second input channel was set up to have a gain of 1 for the samples when ground isolation was needed but a high voltage gate was not necessary. Finally, the last channel was set up with a selectable signal reduction of either 0.1 or 0.01 in order to increase the precision of our gate voltage for sensitive samples. The amplifier is powered by a  $\pm 15V$ ,  $\pm 42V$  floating, linear power supplies, and the device shares the ground with the sample. By connecting two outputs of our 16 bit DAC to the channels with gains 5 and 0.1, we are able to sweep our gate voltage from  $-40V$  to  $+40V$  with steps of  $30\mu V$ .

Our Josephson junction devices utilize lead (Pb) as our superconducting metals. This means that we are unable to anneal our graphene prior to measurement. Even though care was taken to reduce contamination during processing, the Dirac point of our graphene samples was shifted from  $0V$ , in some cases it was shifted by more than  $40V$  and sometimes as high as  $80V$ . In some samples the  $\pm 40V$  sweep of our gate amplifier was not enough to reach the Dirac point of graphene. We have made several battery powered, floating Texas Instrument REF102 based voltage references which are able to add or subtract  $10V$  to a voltage signal. By adding up to four of these voltage references we are able to achieve a gate voltage range of  $\pm 80V$ .

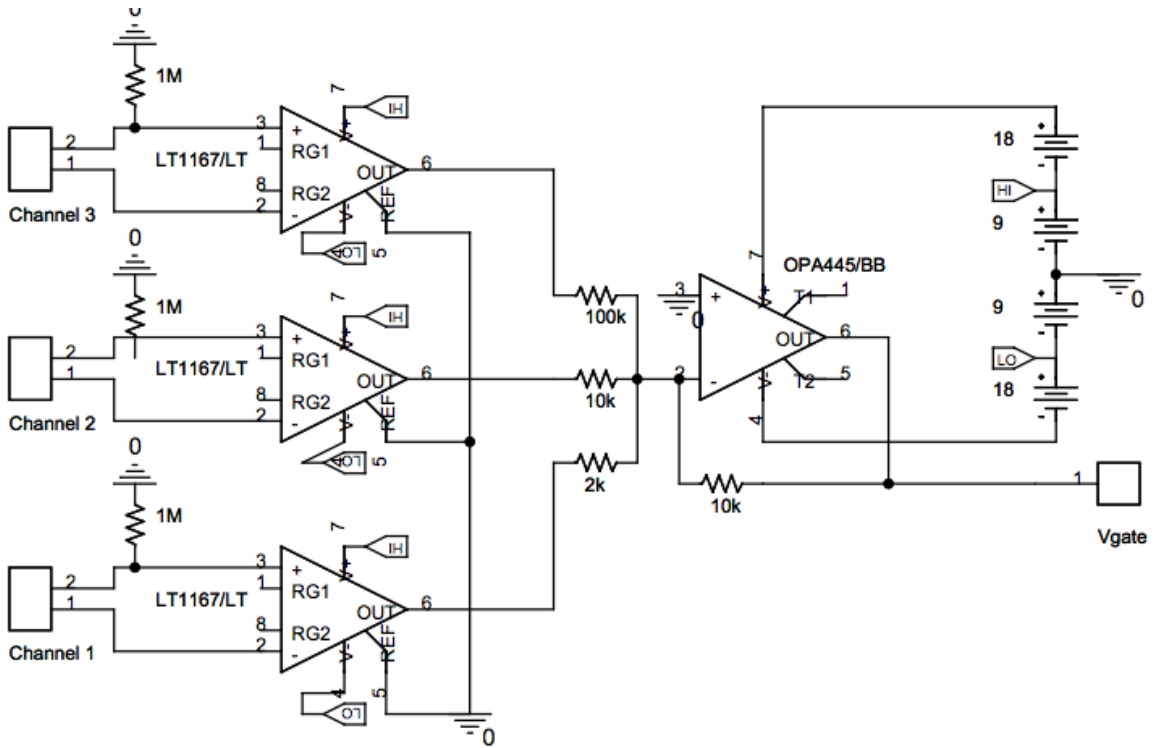


FIGURE 5.6: Schematic of the device used to supply the gate voltage to the sample. This device was made to accomplish three goals: provide a high gate voltage  $\pm 40V$  that is sometimes needed in graphene samples, maintain a fine minimum step in gate voltage despite the possible large total voltage, break the ground between the input signal and the measured sample. Thus, this device was designed as a two-stage summing amplifier. The first stage is made from three instrumental, follower amplifiers (one for each input channel) which buffer the input signal and break the ground between the input and the output. The second stage is a high voltage Texas Instruments OPA445 operational amplifier set up as a summing amp. The first input channel is set up with a gain of 5 which allows up to supply a gate voltage of up to  $\pm 40V$ . The second channel features a gain of 1, while the third channel has a reduction of 0.1 (or in some setups 0.01). This is done in order to reduce the minimum step in voltage provided by the digital to analog converter. By connecting two outputs of our 16 bit DAC to the gain 5 and reduction 0.1 channels of the amplifier we are able to sweep our gate voltage from  $-40$  to  $+40V$  with steps of  $30\mu V$ . The power to the amplifier comes from a  $\pm 15V$ ,  $\pm 42V$  floating, linear power supplies, and the device shares the ground with the sample.

## 5.3 Cryostat Specific Electronics

### 5.3.1 Variable temperature probe

The initial measurements of our graphene based Josephson junctions were taken in a variable temperature probe. During operation, the measured sample is physically submerged into liquid helium, and can have a temperature as low as  $1.4K$ . The electrical contacts to the sample were made using spring loaded, Berillium/Copper pins in order to increase the heat dissipation from the sample as well to eliminate distortions of the applied magnetic field (usually caused by the presence of magnetic materials, such as iron-based spring-loaded pins). We have made all solder connections with large contact areas and used bismuth as the solder material, again, to maintain high heat dissipation.

We have filtered the signals going to the sample by using an array of RC filters located close to the sample and thermally tied to have the same temperature as the sample. These RC filters used  $1nF$  capacitors and a  $4.5k\Omega$  resistor. In order to prevent high frequency noise from bypassing the filters, the input and output ports of each filter were spaced far apart. Finally we encased our filters in stainless steel powder (held together by varnish) which added extra dissipation at high frequencies. The sample itself, was encased in a copper can, however, this shield had several large holes and was therefore not RF tight(39).

### 5.3.2 Dilution Fridge

The later measurements of our samples were taken inside a cryogen free dilution fridge. Due to the significantly lower temperatures, lower cooling power and larger noise associated with cooling motors, as compared to the variable temperature probe, we have taken extra precautions to shield, filter and properly thermalize our sample. The signal from room temperature was sent down to the base temperature of the

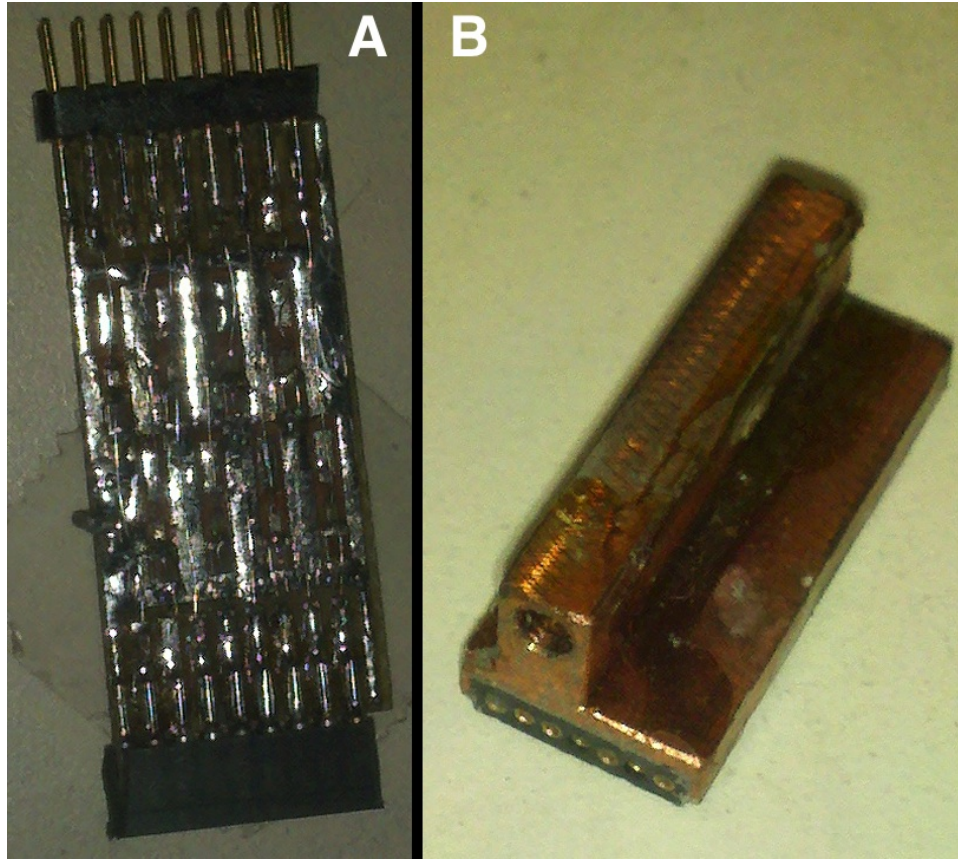


FIGURE 5.7: Every electrical signal that made contact to our graphene based SNS Josephson junction was at the very least filtered by passive RC filters located at the cryostat base temperature. Samples measured in the dilution fridge was in additionally filtered from high frequency noise by the use of resistive, stainless steel coaxial cable leading from the room temperature to the RC filters. Figure A shows an open RC filter bank. The filtering for all 16 channels that could make contact to our sample was shared between two or four filter banks, each bank sharing one circuit board. The filters are made using precision NPO capacitors and metal film resistors. The wiring of filters is surrounded by a ground plane. In case of the filters used in the variable temperature probe cryostat, the top of the filters was covered in stainless steel powder set in varnish. The stainless steel powder acts as additional filtering for very high frequencies that would normally be able to bypass the filter. Shown in Figure B is the filter used in the dilution refrigerator. The top of the filters are enclosed in a copper which is sealed using conductive epoxy. The can, plus the copper plated back of the circuit board housing the filters act as a shield against RF noise as well as reduce the ability of the noise to "hop" across the filter resistance. In addition, the inside of this filter assembly is packed in stainless steel powder to further reduce high frequency noise. The connector of the filters is made to be flat, meaning that when it is installed onto the dilution fridge cold finger, the shielding can of the cold finger and the filters should make electrical contact and seal to prevent RF pickup.

cryostat via a resistive, stainless-steel coaxial cable which acted as filters for high frequency noise as well as thermal isolation. At the cryostat base temperature, the signal was filtered by an array of  $4.5k\Omega$ ,  $1nF$ , RC filters. These filters were placed in copper cans and filled with stainless steel powder in order to further filter high frequency noise.

In order to protect the sample from radio frequency noise, we have designed an RF-tight copper can cold finger. Once closed, the sample is completely encased in a Faraday cage, except for a single sub millimeter diameter capillary installed in order to pump out the enclosure, as well as 32 of  $1mm$  diameter, coaxial feedthroughs which provided the electrical connection to the sample. The feedthroughs are  $1mm$  diameter thru-holes with a depth of  $5mm$ , each with a single pin glued in the middle of the feedthrough. These electrical connections spaced such that the RC filter assemblies were installed directly onto the pins outside the cold fingers and the copper shields of the filters made electrical contact with the copper body of the cold finger. Thus, no physical gap exists that would expose the filtered signal to RF noise(39).

Inside the copper cold finger, the electrical signal was sent through twisted pairs which were wound several times round the central axis of the cold finger as well as encased in stainless steel powder in order to thermalize well to the cold finger. After thermalization, signal wires were wrapped around, crimped and finally soldered with bismuth to Berillium/Copper spring loaded pins which made contact to our samples(40). When using this setup we are able to achieve electron temperatures in our samples as low as  $30mK$ . With the filtering installed, but prior to installing the RF tight, cold finger the electron temperature of our samples was  $60 - 70mK$  inside the dry dilution fridge.

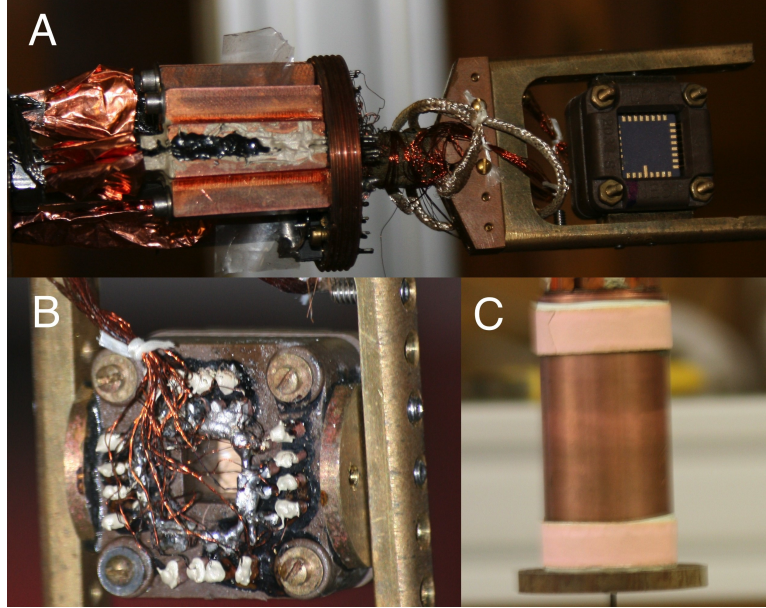


FIGURE 5.8: Photos of the sealed cold finger installed in a dilution refrigerator, designed to shield the measured sample from noise. Figures A and B show the front and back of the cold finger and sample mounts, while Figure C shows the fully assembled and sealed cold finger. Electrical signals reach the cold finger through resistive, stainless-steel coaxial cables which thermally isolate the sample as well as filter high frequency noise. Low frequency noise is filtered by banks of RC filters that are enclosed in copper cans and mounted to the cold finder in such a way that an electrical seal is made between the base of the cold finger and the filter body. The output of the filters is passed into the sealed area of the cold finger using coaxial feedthroughs. Holes are drilled in the cold finger body, each with an individual, isolated pin mounted in the middle. The measured sample is mounted on a PLCC chip and electrical and thermal contact is made by non-magnetic, spring loaded pins. The electrical and thermal contact is made to the pins by copper twisted pairs. In order to make good thermal contact, the wires are wrapped several times around the spring loaded pin and crimped by a copper capillary, thus increasing the thermal contact area. This crimped assembly is in addition soldered using bismuth which unlike regular solder does not become superconducting, and thus retains acceptable thermal conductivity. (Figure B) The twisted pairs are thermalized to the base temperature at the base of the cold finger by winding several times round the copper cylinder in a single layer. The wound wires are glued tight to the cold finger body using stainless steel powder mixed with diluted varnish. Once, the sample is installed, the cold finger assembly is sealed by a copper can. (Figure C) This can is made with a raised inner edge in order to augment the imperfect seal made by the thread. Prior to installing the sealed cold finger, the electron temperature in the cryostat was measured to be 60 – 70mK, which went down to as low as 30mK once the sealed system as utilized.

## Critical Current and Phase Diffusion

In this chapter we discuss the measurements of the switching and retrapping currents in our graphene based Josephson junction and their relationship to the quality factor  $Q$ . In addition we present the observation of the phase diffusion regime in our Josephson junction. We analyze the measurement of zero bias resistance  $R_0$  associated with the phase diffusion regime and find that the data are a good match to theory. (Measurements in the dilution fridge are in progress, hence, we describe only the  $1.4K$  measurements here.)

### 6.1 Introduction

Our graphene based-superconductor-normal metal-superconductor Josephson junctions demonstrate an enhanced zero-bias conductance up to temperatures of the order of 5 K, and at temperatures below  $\sim 2$  K a clearly visible supercurrent branch appears in the  $I-V$  curves. At lowest temperature value in this measurement ( $1.3K$ ) our junctions show hysteretic behavior, meaning that the switching current  $I_S$  (the current above which the Josephson junction switches from the superconducting to the normal state) and the retrapping current  $I_R$  (the current below which the Joseph-

person junction switches from the normal state back to the superconducting state) are different. This hysteresis implies that our junction are underdamped.

In all of our samples, a small, but non-zero voltage is observed below the switching current. We attribute this feature to the phase diffusion mechanism (2). The phase diffusion in underdamped junctions is enabled by the junction's environment, which provides dissipation at high frequencies (23). Observation of this regime in our SGS junctions is facilitated by the high critical temperature of Pb. We first study the phase diffusion resistance as a function of temperature, which allows us to extract the activation energy associated with the phase slips. Next, the phase diffusion is measured at different gate voltages, resulting in a consistent picture of the junction's environment and dissipation at high frequencies. This series of measurements allows us both to establish the phase diffusion regime in underdamped SGS junctions, and to analyze their behavior in terms of well-established models. Finally, we demonstrate an efficient way of controlling the junction by passing a current through one of the electrodes within the same structure: the locally created magnetic field modulates the critical current. Several periods of oscillations are visible, indicating the spatial uniformity of the junction.

## 6.2 Quick Review and Sample Parameters

Josephson junctions with a normal metal region sandwiched between two superconductors are known as superconductor-normal-superconductor (SNS) structures. The normal region has been made from non-metallic nanostructures, including heterostructures, nanotubes, quantum wires, quantum dots (41), and, most recently, graphene (31; 42; 30; 43). Usually, these superconductor-graphene-superconductor (SGS) junctions employ aluminum as the superconducting metal, separated from graphene by another metal layer (often titanium) intended to create a good contact. However, we designed a process to make palladium-lead (Pd/Pb) contacts to

graphene. Pd is known to form low-resistance contacts to graphene (36; 37), while Pb has the advantage of a relatively large critical temperature (7.2 K).

Graphene was prepared by a version of the conventional exfoliation recipe (7) from natural graphite stamped on RCA-cleaned Si/SiO<sub>2</sub> substrates. The samples were verified by Raman spectroscopy to be single atomic layer thick with low defect density (35). The electrodes were patterned by standard e-beam lithography and thermal evaporation. We first deposited  $\sim 2$  nm of Pd, which formed highly transparent contacts to graphene (36; 37), followed by  $\sim 70$  nm of Pb. Care was taken not to heat the samples above  $\sim 90^\circ\text{C}$ , and to store them in vacuum in order to minimize oxidation of Pb.

The inset of Figure 6.1 shows a scanning electron micrograph of a typical device. A layer of graphene is visible as a gray triangular-shaped shadow in the center of the image, contacted by two long metallic electrodes. A known current (AC + DC) is driven through the graphene between two probes on one side of the sample, and voltage is measured between two probes on the other side. We present the results measured on three different samples. Sample A has a gap of  $d = 100$  nm between the leads; the graphene region is  $L = 1.5\mu\text{m}$  long. In samples B and C, the leads meander across graphene for a much longer total distance of  $L \sim 15\mu\text{m}$  and  $\sim 20\mu\text{m}$ , respectively. The gap between the leads is designed to be  $d = 500$  nm (B) and 400 nm (C).

### 6.3 Critical Current and Phase Diffusion

Figure 1(a) demonstrates the simultaneously measured DC voltage  $V$  and differential resistance  $dV/dI$  vs. applied current  $I$  in sample A. (The inset shows a different sample of a similar design.) From the  $dV/dI$  curves, it is clear that a pronounced effect of superconductivity is observed at temperatures as high as  $\sim 5$  K, which is comparable to the transition temperature of the leads (verified to be  $\approx 7$  K). At

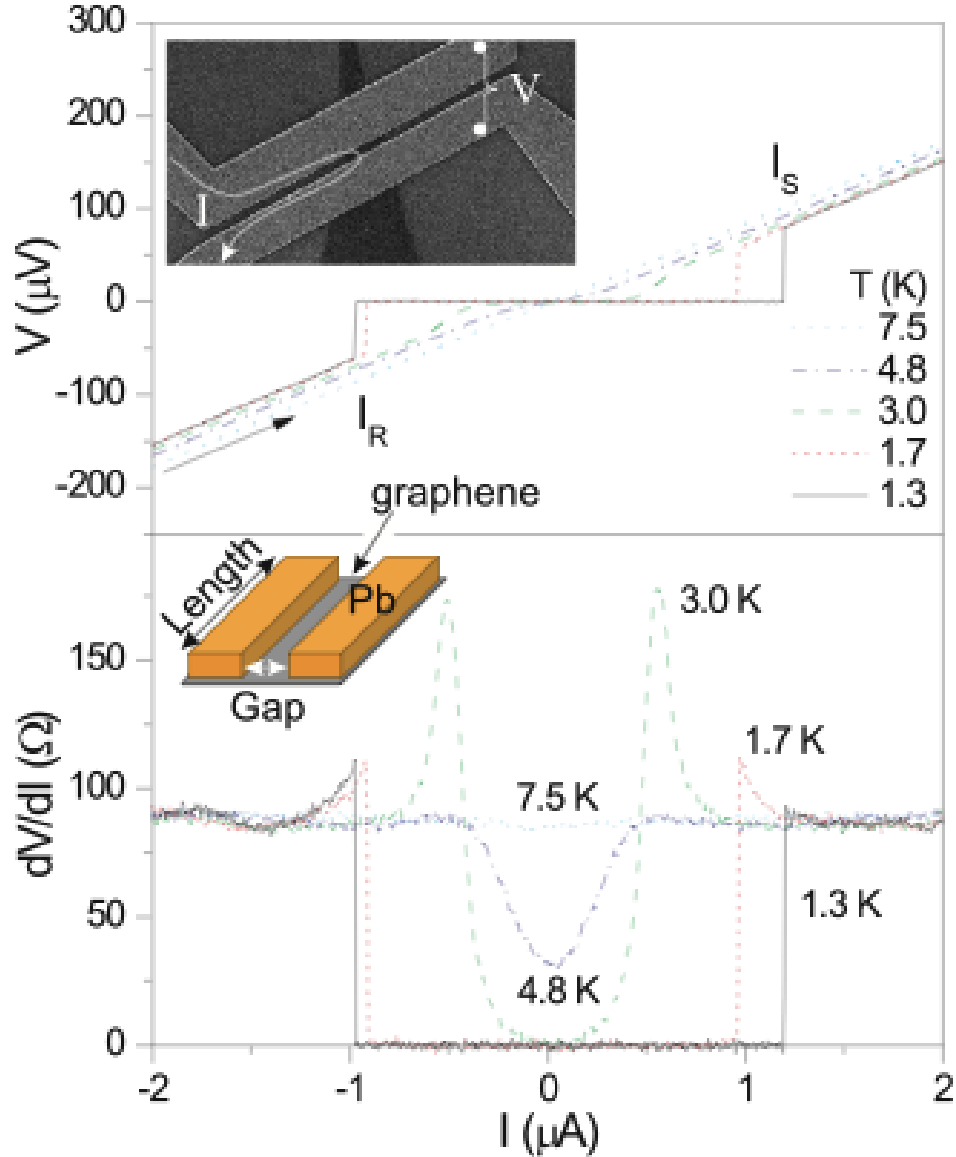


FIGURE 6.1: Inset: scanning electron micrograph of a typical sample and the measurement schematic. Two Pd/Pb contacts are made to graphene (gray triangular shade). A fixed DC current  $I$  with a small AC modulation (tens of nA) is driven through graphene between contacts on one end of the sample, and the voltage drop  $V$  is measured between two contacts on the other end. Bottom inset: schematic showing the sample layout and defining dimensions. Main panel: DC voltage  $V$  and differential resistance  $dV/dI$  vs. bias current  $I$  measured at several temperatures on sample A (different from the sample shown in the inset).  $V_{gate} = +40$  V is applied to enhance the conductance of graphene. Each curve is measured while sweeping the current from negative to positive, resulting in hysteresis at the lower temperatures, at which a difference appears between the switching and retrapping currents. (The spikes in  $dV/dI$  at the switching and retrapping currents are naturally truncated in the measurement.)

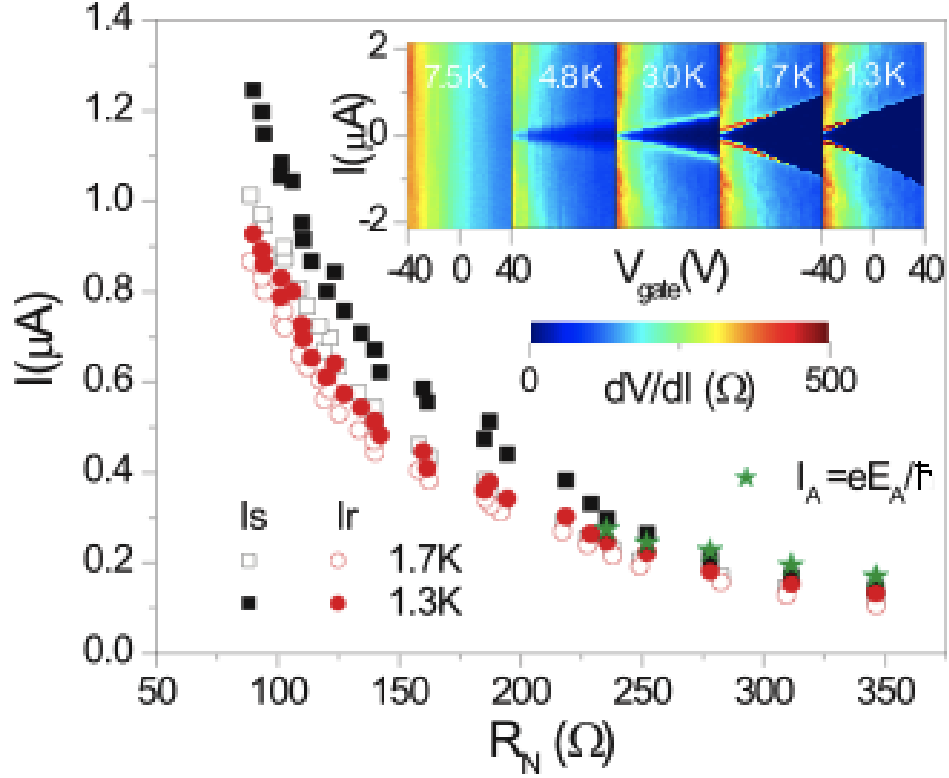


FIGURE 6.2: Switching and retrapping currents ( $I_S$  and  $I_R$ ) as a function of  $R_N$ , which is controlled by the gate voltage. The normal resistance is extracted from the  $I - V$  curves as  $dV/dI$  at a current of  $2\mu A$ , exceeding the switching current; thus defined  $R_N$  virtually does not depend on temperature. Stars: critical current extracted as  $I_A = eE_A/\hbar$  from the activation energy  $E_A$  of phase diffusion (see Figure 2 for more details). Inset: maps of  $dI/dV$  vs.  $I$  and  $V_{gate}$  at 5 different temperatures.

the two lowest temperatures, the  $I - V$  curves show a region of vanishing small  $V$ ; the junction abruptly switches to a normal state when the current exceeds a certain value (the switching current,  $I_S$ ). On the reverse current sweep, voltage drops close to zero at the retrapping current ( $I_R$ ). Figure 6.2 plots  $I_S$  and  $I_R$  at the two lowest temperatures vs. the normal resistance of the sample, controlled by  $V_{gate}$ .

Observation of the hysteresis in the  $I - V$  curves indicates that the junction is underdamped (2). Indeed, the estimated quality factors of our junctions are of the order of one (see also the discussion of Figure 6.4). Here, we take into account

the presence of the degenerately doped Si substrate, which provides the dominant contribution to the capacitance between the superconducting leads (tens of fF). An alternative explanation of hysteresis in a SNS junction could be overheating (44). In our case, two samples (A and C) have very similar switching and retrapping currents. Their normal resistances, which control the heat generation just before the retrapping, are different only by a factor of  $\sim 2$ . However, the dimensions of graphene regions, which control the heat dissipation, are vastly different: the areas differ by  $\sim 50$ , and the contact lengths differ by  $\sim 15$ . Therefore, conventional underdamping, rather than overheating, seems more likely in our case.

In all our samples, a finite voltage on a  $\mu\text{V}$  scale appears on the superconducting branch of the  $I - V$  curve. This behavior is illustrated in Figure 6.3a, showing the  $I - V$  curves measured in sample B at three different temperatures, including 1.4 K, at which the  $I - V$  curve is hysteretic. The appearance of a finite voltage is explained by the “phase diffusion” mechanism, where a point representing the phase slowly descends the tilted washboard potential (2), getting trapped at successive local minima following each phase slip. The existence of the phase diffusion regime in an *underdamped* junction indicates an efficient high-frequency dissipation due to the junction environment (23). Experimentally, we find that the measured values of the switching current are reproducible upon successive sweeps, again supporting the phase diffusion mechanism as opposed to premature switching by a single phase slip (2). While not yet reported in graphene, the phase diffusion regime has been recently analyzed in a conceptually similar case of an underdamped junction based on a multiwall carbon nanotube (45).

The presence of phase diffusion allows us to investigate the rate of phase slips, proportional to the sample resistance, and its dependence on temperature. Theoretically, the zero-current differential resistance due to the phase diffusion should depend

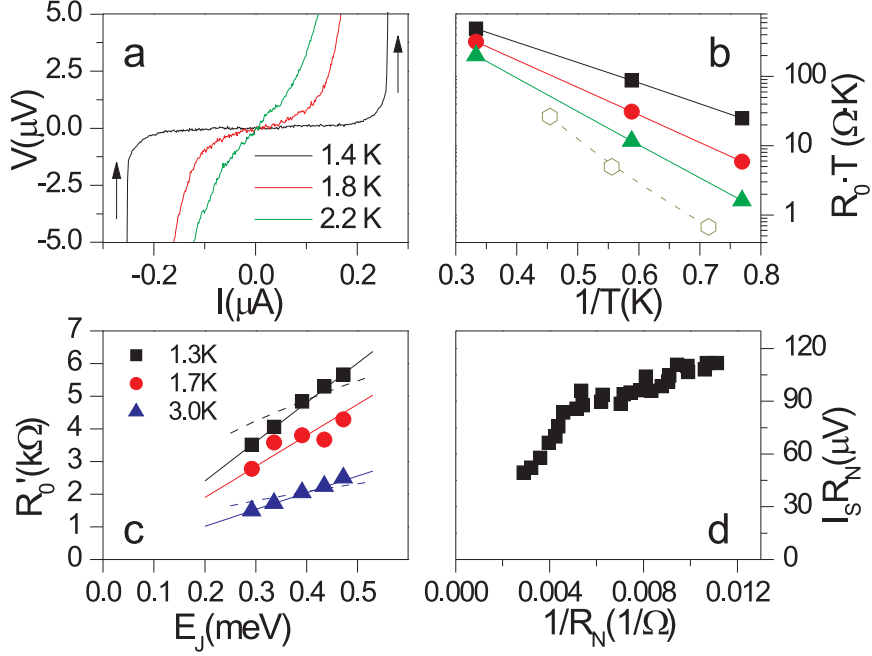


FIGURE 6.3: a)  $I - V$  characteristics of sample B at several temperatures and  $V_{gate} = 0$ . Finite voltage could be noticed *below* the switching current at the lowest temperature. b) The product of the temperature times the differential resistance,  $TR_0$ , as a function of inverse temperature  $1/T$ , measured on sample A (filled symbols), and on sample B (empty symbols). In sample B,  $V_{gate} = 0$ , while in sample A, several values of  $V_{gate}$  are taken, resulting in several sets of symbols. Evidently, in all sets,  $TR_0$  demonstrates activation behavior, with an activation energy of  $E_A \sim 10$  K. This energy is converted to critical current according to  $I_A = eE_A/\hbar$ , shown by stars in Figure 1(b). (The differential resistance at small current,  $R_0(T)$ , becomes too small to measure at low  $R_N$ , so the analysis is limited to the high- $R_N$  range.) c) Symbols: the prefactor to the exponential,  $R'_0$  (see text), *vs.*  $E_J$  extracted from the same data as in panel (b). Lines are a linear fit, assuming  $R'_0 \sim Z_0 E_J/k_B T$ , which corresponds to a junction underdamped at DC but overdamped at the plasma frequency. For comparison, the dashed lines illustrate the expression  $R'_0 \propto \sqrt{E_J}$ , which clearly does not fit the data well. d) The product of the switching current and the normal resistance  $I_S R_N$  *vs.* inverse resistance  $1/R_N$ .

on temperature as (19; 20; 21; 23; 22)

$$R_0(T) \propto T^{-1} \exp(-2E_J/k_B T). \quad (6.1)$$

Here, the Josephson energy  $E_J = \hbar I_C^{(0)}/2e$ , and  $I_C^{(0)}$  is the true critical current of the junction. Figure 6.3(b) shows the product  $TR_0(T)$  plotted as a function of the inverse temperature for samples A and B. Both samples clearly show activation behavior; the extracted activation energy turns out to be close to twice the Josephson energy, as estimated from the switching current. This is illustrated in Figure 6.2, where for the ease of comparison we convert the activation energy  $E_A$  to current as  $I_A = eE_A/\hbar$  (stars), which is indeed close to  $I_S$ .

We now analyze the dependence of the phase diffusion resistance  $R_0$  on  $E_J$ , controlled by  $V_{gate}$ . Let us define the prefactor to the exponential in eq. (6.1) as  $R'_0 \equiv R_0 e^{2E_J/k_B T}$ . Theoretically, this prefactor varies depending on whether the Josephson junction is overdamped or underdamped. For an overdamped junction,  $R'_0 \sim RE_J/k_B T$  (20; 21), where  $R$  is the shunting resistance, *i.e.*  $\sim R_N$ . In case of an underdamped junction,  $R'_0 \sim \frac{\hbar}{e^2} \hbar \omega_P / k_B T$  (23), so that  $R'_0$  depends on  $E_J$  and the junction capacitance  $C$  through the plasma frequency  $\omega_P \propto \sqrt{E_J/C}$ . Finally, if the junction is underdamped at DC, but overdamped at the plasma frequency,  $R'_0$  scales as  $\propto Z_0 E_J / k_B T$ , where  $Z_0$  is the real part of the impedance of the junction's environment at high frequency (22).

Since  $C$  and  $Z_0$  do not change with the gate voltage, while  $R_N$  and  $E_J$  do, we may distinguish between the different cases. In Figure 6.3(c), we plot  $R'_0 \equiv R_0 e^{2E_J/k_B T}$  vs.  $E_J$  (taken as  $E_A/2$ ) for three temperatures, 1.3, 1.7, and 3.0 K. It is clear that the scaling of  $R'_0$  is consistent with  $\propto E_J$  and is not consistent with either  $R'_0 \propto \sqrt{E_J}$  or  $R'_0 \propto R_N E_J$  (not shown) (46). This observation allows us to identify the junction as underdamped at DC, with plasma frequency oscillations damped by the environment; the environmental impedance is found to be  $Z_0 \approx 200 - 250 \Omega$ . The overall agreement

convinces us that the macroscopic behavior of the junction is adequately described by Ref 18.

Using Ref. 18 we estimate that at  $T = 1.3$  K,  $I_S$  is close to  $I_C^{(0)}$  (exceeds 70% for the whole range shown in Figure 6.2). Therefore, we can use  $I_S$  in place of  $I_C^{(0)}$  and plot  $I_S R_N$  vs.  $1/R_N$  in Figure 6.3(d). The trend in the graph resembles that of  $I_C^{(0)} R_N$  vs. the Thouless energy,  $E_{Th}$ , as expected in the SNS junctions (28). Indeed,  $E_{Th}$  should be inversely proportional to the resistivity of graphene. At the location of the “knee” in the curve,  $E_{Th}$  is estimated to be of the order of  $\Delta$ , indicating the transition between the ballistic and diffusive SNS regimes. We do not attempt a more careful comparison of these preliminary data with theory, since extracting  $E_{Th}$  from  $R_N$  would require the exact knowledge of the contact resistance and the density of states in the sample. Also, the superconducting gap is likely suppressed at the interface, which would complicate analysis.

## 6.4 Application of Small B-Fields and Quality factor analysis

We will now discuss the effects of magnetic field on the junctions. In order generate the field, we passed a large (mA range) DC current  $I_L$  along one of the Pb leads, parallel to the interface with graphene. For these measurements, we picked relatively large pieces of graphene, and made the junction’s length  $L$  tens of  $\mu\text{m}$  by meandering the leads across the sample surface (samples B and C). The resultant large area between the leads allowed us to pass several flux quanta through graphene, before  $I_L$  drove the Pb lead normal.

Figure 6.4a shows the DC voltage drop across graphene  $V$ , mapped as a function of the current  $I$  flowing through graphene, and the current  $I_L$  generating the magnetic field. Several regions of vanishing voltage are visible along the horizontal axis. From the extent of these regions, one can extract the switching and retrapping currents,  $I_S$

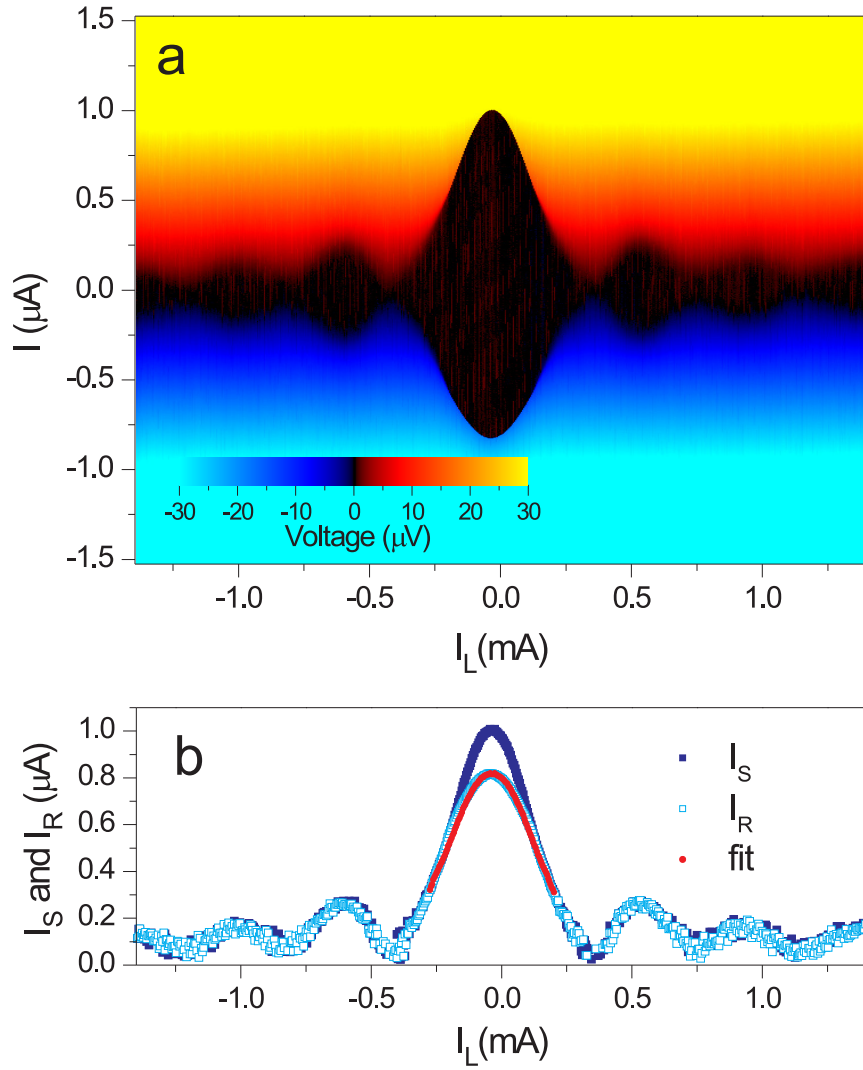


FIGURE 6.4: (a) Map of the voltage drop  $V$  measured *vs.* bias current  $I$  and the current  $I_L$ , which flows along one of the leads parallel to the interface with graphene and induces magnetic field  $B_L$ . The dark regions along the horizontal axis correspond to the supercurrent branch. The current is swept from the negative to the positive direction, resulting in the visible hysteresis between the retrapping (negative  $I$ ) and switching (positive  $I$ ) currents in the central lobe. (b) Extracted switching and retrapping currents *vs.*  $I_L$ .  $T = 1.3$  K,  $V_{gate} = 40$  V.

and  $I_R$ , vs.  $I_L$  (Figure 6.4(b)). The resulting modulations are close to the expected Fraunhofer pattern  $I \propto \sin(\pi I_L/I_{L,0})/I_L$  (2), where  $I_{L,0}$  corresponds to passing one flux quantum through the junction. Observation of several oscillations (about 5 at both positive and negative  $I_L$ , not shown) indicates a uniform junction. We also found that similar modulation are induced by an externally applied magnetic field, as reported previously in other S-graphene-S samples (31; 42; 30; 43).

The difference between  $I_S$  and  $I_R$ , which exists in the center of the pattern in Figure 6.4a, disappears at higher magnetic field, *i.e.* for lower  $I_S$ . For example, it is not seen in the side lobes at all (Figure 6.4b). This implies that the quality factor  $Q(I_C^{(0)}) = (2eI_C^{(0)}C/\hbar)^{1/2}R$  is close to 1 at the central lobe. Assuming that other parameters of the junction, except for  $I_C^{(0)}$ , do not depend on magnetic field, we may fit  $I_R$  as  $f(Q)I_C^{(0)}$ , where  $f(Q)$  is a universal function, approximated at  $Q \sim 1$  as  $f(Q) \approx 1.273 - 0.311Q - 0.030Q^2 + 0.013Q^3$  (18). We can further replace  $I_C^{(0)}$  with the measured  $I_S$  (see *e.g.* (48)) – indeed, based on Ref. 39 the two currents are estimated to be very close for  $I_S \gtrsim 0.4\mu\text{A}$  at  $T = 1.3\text{ K}$ , as we have already discussed for sample A. The fit shown in Figure 6.4(b) is achieved by taking  $Q = 1.4$  at the center of the pattern as the only fitting parameter. As expected from the theory (18), the difference between  $I_R$  and  $I_S$  disappears at  $Q \approx 0.85$ .

## Non-trivial Effects of Magnetic Field

In this chapter, we further look at the effects of magnetic field on our graphene based SNS Josephson junctions. We observe deviations from the canonical Fraunhofer interference pattern. We attribute the causes for such deviations to our non trivial sample layout, and we run simulation to support this claim.

### 7.1 Sample and Measurement Design

Just as for the previously discussed samples, the superconducting contacts to graphene are made from a Palladium/Lead (Pd/Pb) bilayer. First, we deposit a 2 nm layer of palladium, which creates transparent contacts to graphene (36; 37); 100nm layer of lead is deposited in situ on top. The lateral width of the contacts is 500 nm. Unlike the samples in chapter 6, here we present the results measured on a large junction: about  $20\mu\text{m}$  wide and 400 nm long. In order to create such a wide junction, the leads are bent in two places to fit on a moderately-sized graphene flake (Fig. 7.1). We see that this particular sample design has certain nontrivial consequences.

We measured the sample electronic properties using a pseudo 4-probe setup (Fig. 7.1). The junction is biased by current  $I$  which contains a small AC component,

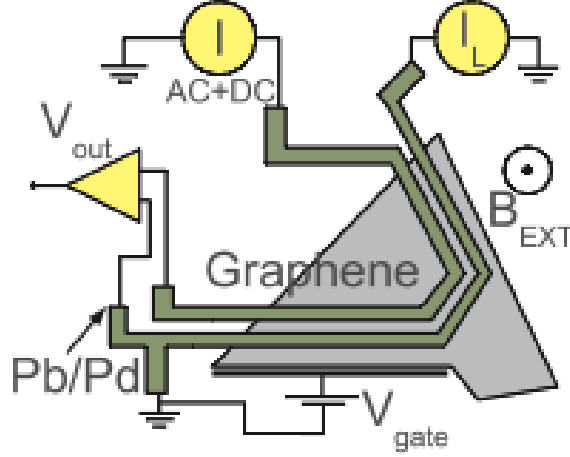


FIGURE 7.1: Schematic of the measurement setup. The metal leads form a “ $\sqcup$ ” shape in order to increase their length. Bias current  $I$  with a small AC modulation is sent through the junction. The resulting AC component of the voltage across the junction is measured using a lock-in amplifier allowing one to record the differential resistance  $R \equiv dV/dI$ . An external magnetic field  $B_{ext}$  is applied by a superconducting solenoid. In addition, a magnetic field  $B_L$  is created by sending a current  $I_L$  along one of the Pb leads of the junction. Sweeping the current  $I_L$  allows to apply a very small magnetic field  $B_L$ .

and the AC voltage across the junction is measured using a lock-in amplifier. The carrier density in graphene can be tuned by the back-gate voltage  $V_{gate}$  but for the results presented the gate voltage is set at zero. Finally, a perpendicular magnetic field can be applied using two methods. Conventionally, a field  $B_{ext}$  can be created by an external solenoid magnet. Alternatively, we send a current  $I_L$  along one of the superconducting leads (Fig. 7.1), inducing a field which we label as  $B_L$ . The advantage of the second method is that the required small fields can be easily obtained and rapidly changed. In this sample we have calibrated  $B_L$  to be equal to  $0.95 \frac{T}{A} I_L$  (see details below).

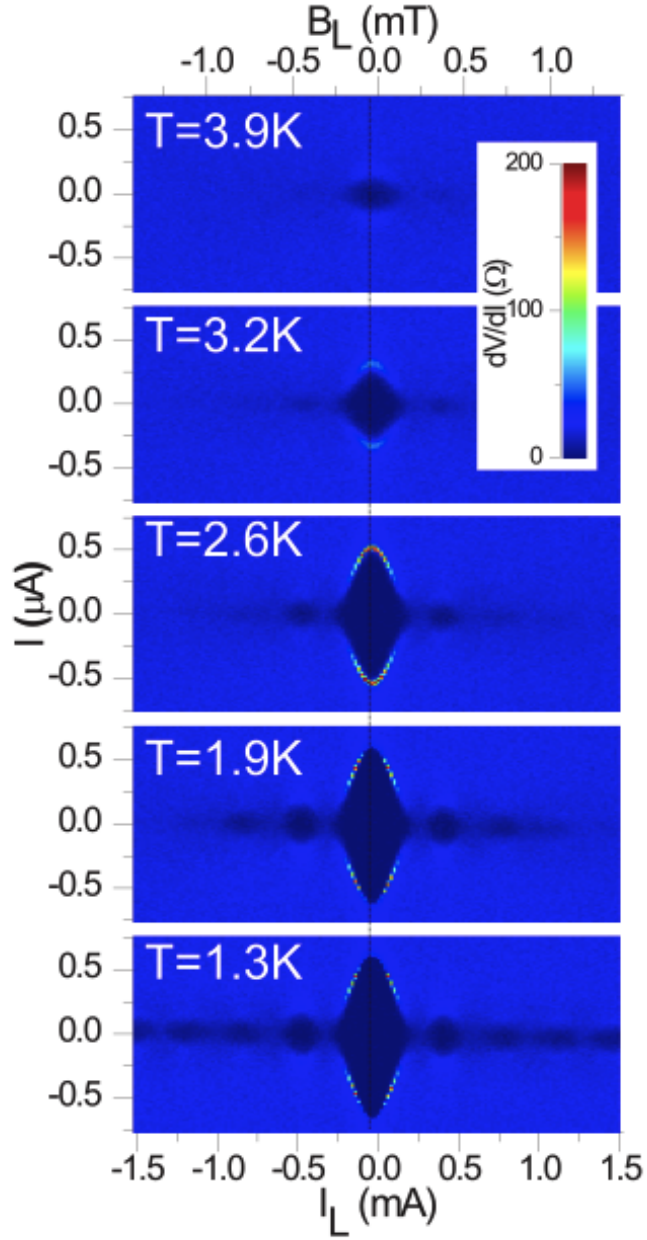


FIGURE 7.2: Differential resistance  $dV/dI$  maps measured *vs.* bias current  $I$  and magnetic field-inducing current  $I_L$ . Regions of vanishing  $R$  appear dark. Each panel corresponds to measurement at a different temperature. Enhanced zero-bias conductance develops around  $\approx 4K$  for small fields  $B_L$ . With lower temperatures more and more critical current modulations appear and the Fraunhofer interference pattern is observed. At the base temperature of  $1.3K$ , critical current is seen at fields beyond  $5mT$  (see Figure 5). Observing many oscillations suggest that the junction is highly uniform.

## 7.2 Results

As with the samples discussed in chapter 6, Pd/Pb electrodes become superconducting at a temperature of  $\approx 7$  K, and the SGS junctions begin to exhibit enhanced zero-bias conductance at temperatures of  $\approx 5$  K. Below  $\approx 2$  K, a fully formed supercurrent branch is clearly observed (49). Figure 1c demonstrates the differential conductance  $R \equiv dV/dI$  versus bias current  $I$  (vertical axis) and magnetic field  $B_L$  (horizontal axis) measured at several temperatures. The dark areas of the maps in Figure 1c correspond to the regions of suppressed resistance. The regions are bound by a critical current  $I = I_C$ , above which the junction becomes normal. The value of  $I_C$  increases as temperature is lowered and saturates around  $I_C \approx 0.5\mu\text{A}$  at zero magnetic field (see the lowest map in Fig. 7.2). When  $B_L$  is applied,  $I_C$  oscillates in a way closely resembling the Fraunhofer diffraction pattern (2). Several oscillations of  $I_C$  can be observed at the lowest temperature; this indicates that the junction is uniform.

We next apply an external magnetic field  $B_{ext}$ , which is found to shift the modulation pattern of Figure 7.2 in the horizontal direction (Fig. 7.3). The shift is linear in  $B_{ext}$ : indeed, at the center of the pattern the external field and the one induced by  $I_L$  cancel each other. The observed rate of shift allows us to fix the conversion  $B_L = 0.95 \frac{\text{T}}{\text{A}} I_L$  mentioned earlier. This factor is also consistent with our order of magnitude estimates. Furthermore, the shift of the pattern by  $\Phi_0$  in an external magnetic field of 0.36 mT allows us to extract the effective area of  $5.6\mu\text{m}^2$ . While this area is smaller than the  $8\mu\text{m}^2$  expected from the designed sample dimensions of  $W = 20\mu\text{m}$  by  $L = 0.4\mu\text{m}$ , it is quite likely that the length  $L$  between the leads is reduced in the process of lithography, or that the magnetic field is modified due to the presence of the superconducting leads.

When magnetic field  $B_{ext}$  of the order of tens of mT is applied to the sample, the

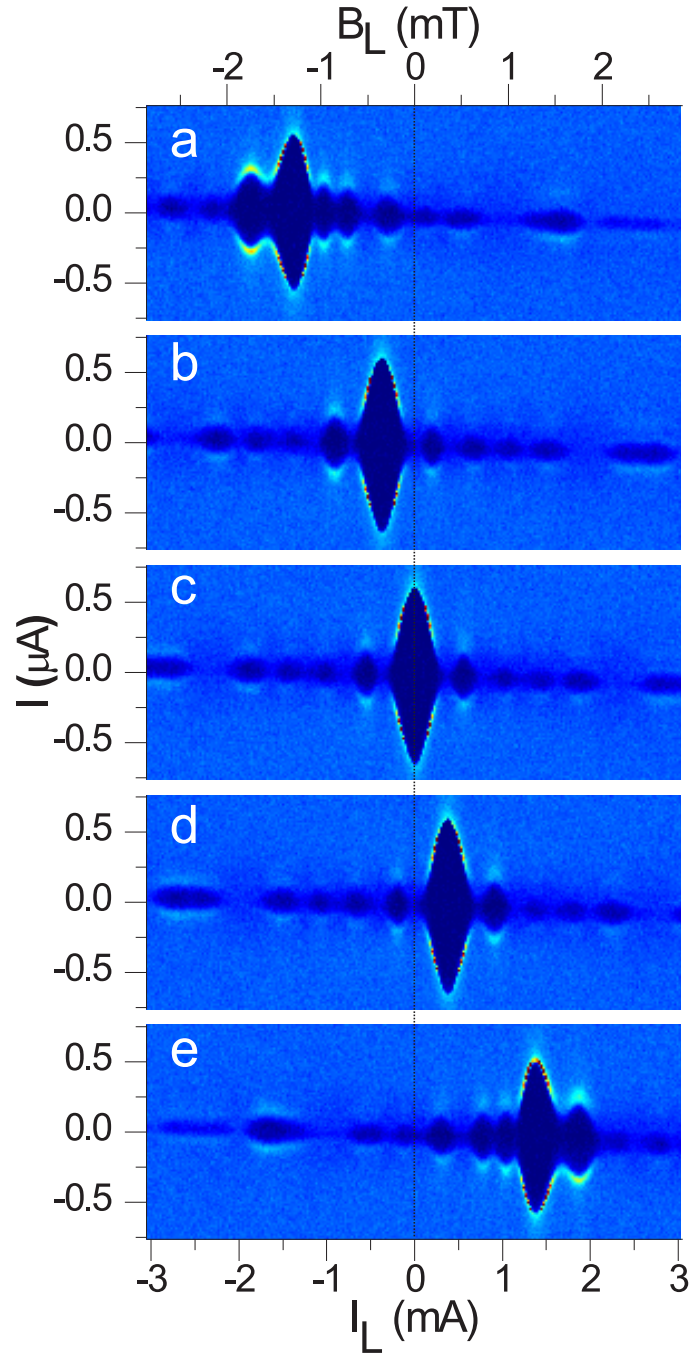


FIGURE 7.3:  $R(I, I_L)$  maps (like those in Fig. 1c) measured at different values of the external magnetic field (a):  $B_{ext} = -1.3$  mT, (b):  $B_{ext} = -0.36$  mT, (c):  $B_{ext} = 0$ , (d):  $B_{ext} = 0.36$  mT, (e):  $B_{ext} = 1.3$  mT. Application of  $B_{ext}$  shifts the modulation pattern, so that at its center  $B_{ext}$  and  $B_L$  cancel each other (b-d). Since the cancellation is not perfect, the pattern gets distorted (a), compared to the pattern at zero external field (c). An opposite orientation of the external magnetic field (e) results in mirror reversal of the distortions.  $T = 1.3$  K.

observed pattern becomes distorted even after the field is returned back to zero (Fig. 7.4). It is clear that the resulting pattern at  $B_{ext} = 0$  (Fig. 7.4a) is very different from the original one (Fig. 7.3c). We can partially recover the original pattern by setting  $B_{ext} \approx 3.4\text{mT}$  (Fig. 7.4b). When comparing the resulting pattern to the original one (Fig. 7.3c), we notice that the critical current is slightly suppressed and the side-lobes have somewhat random heights. We attribute these distortions and the shift from zero field to the trapping of magnetic flux in the superconducting film (50). Indeed, the undistorted pattern seen in Figure 7.3c can be restored following the thermal cycling to  $\approx 10\text{K}$ , beyond the critical temperature of lead.

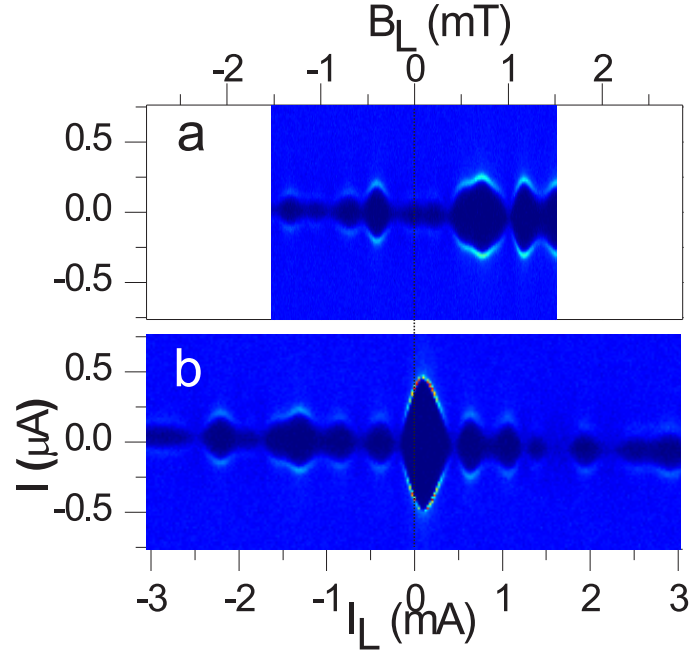


FIGURE 7.4:  $R(I, I_L)$  measurements taken after the perpendicular magnetic field was ramped beyond several tens of mT. Panel (a) shows the measurement done when  $B_{ext}$  was returned back to zero. Clearly, the pattern is now vastly distorted. Panel (b) is taken at  $B_{ext} = 3.4\text{mT}$ . At this field, the original critical current modulation pattern (Fig. 2c) is partially restored. However, the central lobe shows a suppressed critical current, and the side-lobes form a distorted pattern. These permanent distortions are attributed to trapped flux in the Pb leads. Heating of the sample beyond the  $T_C$  of Pb is required in order to restore the symmetric patterns seen in Figure 2c.

Interestingly, at fields less than those causing trapped flux of Figure 7.4, distortions of a different nature are introduced to the pattern (Fig. 7.3a). The first difference is that, returning to  $B_{ext} = 0$  restores the original pattern without any hysteresis. Second, the pattern demonstrates perfect symmetry under simultaneous reversal of both  $B_{ext}$  and  $I_L$ , compare Figures 7.3 (a) and (e). We associate this behavior with the fact that the phase difference is not linear along the length of the leads. Indeed, the field  $B_L$  may not be entirely uniform, so that it is not perfectly compensated by  $B_{ext}$ . Most likely, the deviations of  $B_L$  from uniformity are caused by the bends in the leads (schematic in Fig. 7.1), at which points the phase difference experiences discontinuous steps proportional to  $I_L$ . The situation is very similar to the junctions with an artificial phase discontinuity controlled by an external current (52; 51). Indeed, some of the features we observe in Figures 7.3(a) and (e), *e.g.* the strengthening of the side lobe at the expense of the central lobe, resemble those found in Refs. (52; 51).

### 7.3 Simulation

To describe the distortions found in Figure 7.3a,e, we consider a semi-realistic model of the sample. We assume that the leads extend from  $x = -W/2$  to  $+W/2$ ; the position-dependent phase difference  $\Phi_L(x)$  (induced by  $B_L(x)$ ) is taken to be piecewise linear in  $x$ , with a slope proportional to  $I_L$ . Two identical discontinuous steps of  $\Phi_L(x)$  are placed at  $-W/10$  and  $+W/10$ . The strength of the discontinuities is taken to be also proportional to  $I_L$ . These points are close to the actual locations of the bends in the leads, but we checked that the main features of the simulation do not crucially depend on the details (*i.e.* the position of discontinuities or symmetry of their placement).

We also include the effect of the external field, presuming it induces uniform phase difference  $\Phi_{ext}(x)$  along the length of the leads. In our simulations, the current-phase

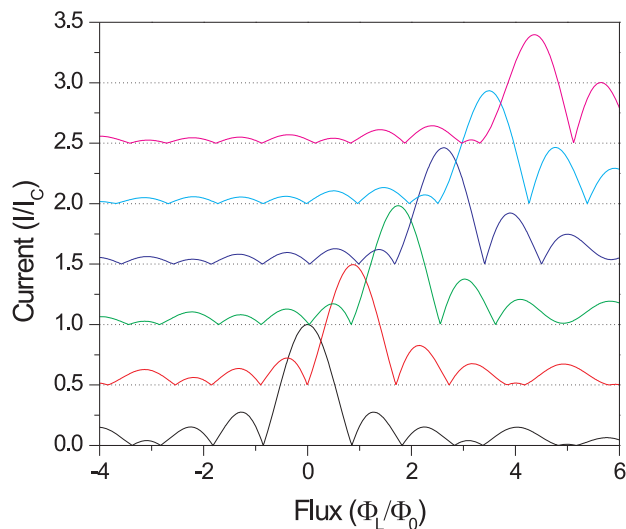


FIGURE 7.5: Simulated critical current vs.  $I_L$  at several values of  $B_{ext}$ . The bottom curve is taken at  $B_{ext} = 0$ , and in each consecutive curve the external flux grows in units of flux quantum  $\Phi_0$ . The phase difference between the two leads induced by  $I_L$  is assumed to grow linearly along the length of the leads, proportionally to  $I_L$ , and to step discontinuously at two locations by an amount also proportional to  $I_L$ . This particular functional form it chosen to approximate the realistic shape of the sample, where the leads turn  $90^\circ$  in two places; however the major features appear insensitive to the exact locations of the discontinuities. The horizontal axis is labeled in units of total flux  $\Phi_L$  induced by  $I_L$  excluding the discontinuities. The additional phase jump at each discontinuity is equal to  $0.1\pi\Phi_L/\Phi_0$ .

relation is assumed to be sinusoidal. Although deviations from a sinusoidal relation have been recently observed in SGS junctions (53), the approximation should be adequate in our case, due to the relatively large distance between the leads ( $L = 400$  nm) and the relatively high temperature 1K.

The simulated patterns of the critical current  $I_C$  vs.  $I_L$  and  $B_{ext}$  are shown in Figure 7.5. The main features observed in Figure 7.3 are qualitatively reproduced, such as: 1) the overall shift of the  $I_C(I_L)$  pattern in  $B_{ext}$ ; 2) the growing distortion of the  $I_C(I_L)$  pattern in  $B_{ext}$ ; 3) the growing strength of the side lobe on the high current side of the pattern at the expense of the central lobe; 4) the difference in

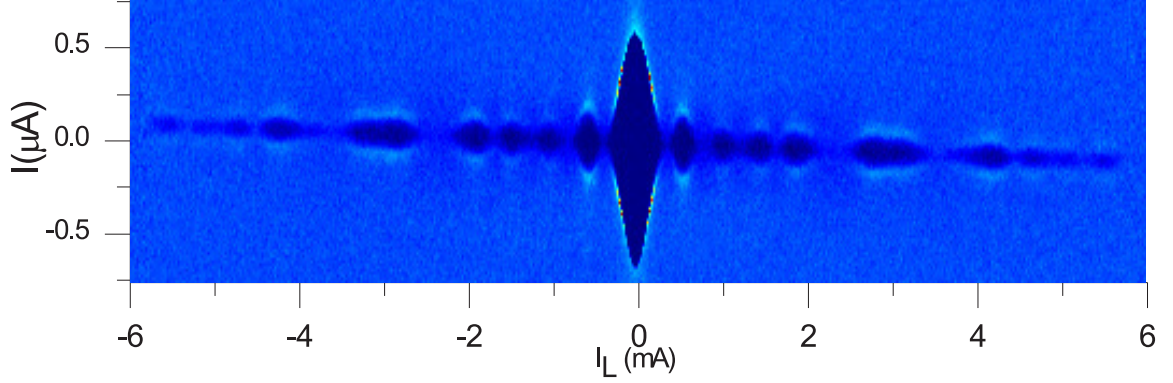


FIGURE 7.6: Differential resistance  $dV/dI$  map measured *vs.* bias current  $I$  and current  $I_L$  inducing magnetic field. These data are similar to Fig. 2c, but is extended up to  $I_L = 6mA$ . Note the suppression of select side-lobes (see  $I_L \approx \pm 2.5mA$  and  $\pm 3.5mA$ ). This suppression of side-lobes qualitatively resembles the simulation results (Fig. 4,  $B_{ext} = 0$ ,  $\Phi_L/\Phi_0 \approx \pm 3$  and  $\pm 5$ ). The tilt of the pattern is an artifact of  $I_L$  flowing through the normal part of the sample, thus creating a voltage drop that shifts the zero of  $I$ .

width between that side lobe and the side lobes on the other side. Moreover, even the  $B_{ext} = 0$  curve, while similar to the perfect Fraunhofer pattern  $I \propto \sin(\pi I_L/I_L^{(0)})/I_L$ , bears noticeable differences. Namely, some of the side lobes are suppressed almost to zero, while further lobes at higher  $I_L$  regain strength. This type of behavior is indeed observed in experiment (Fig. 7.6). Note the region of suppressed critical current at  $I_L \approx \pm 2.3mA$  in Figure 7.3c, and its reappearance at higher  $I_L \approx \pm 3.5mA$ .

## Conclusion and Future plans

### 8.1 Conclusion

We have designed a method for making lead (Pb) contacts to a single layer graphene crystal. An electrically transparent contact is made by the use of a thin palladium contact layer, while a method of thermal evaporation allows for Pb leads to be as little as  $300nm$  wide and  $80nm$  tall with a length of tens of microns while still maintaining a superconducting state. As a result, we observe a suppression of resistance in our Superconductor-Graphene-Superconductor junctions at temperatures as high as  $5K$ .

The higher transition temperature allows us to measure samples that are fully submerged in liquid helium thus eliminating the effect of overheating. At the same time, we see the temperature effects on the switching current saturate as we reach a base temperature of  $1.4K$ . Thus, we are able to observe a hysteresis between the switching and retrapping currents and attribute it to our Josephson junction being underdamped. Our analysis of the quality factor of our junction is found in agreement with the calculations from design parameters.

We are able to observe a non-zero resistance of our Josephson junction even at

vanishing bias current and attribute it to the regime of phase diffusion. By studying the zero bias resistance  $R_0$  versus temperature in the phase diffusion regime we are able to extract the Josephson energy  $E_J$ . The extracted Josephson energy is found to be in agreement with the value obtained from the direct measurements of the switching current. By changing the gate voltage applied to the graphene layer, we are able to conclude that the phase diffusion regime observed in our samples is caused by the junction becoming overdamped at high frequencies due to the shunting effects of the environment. We extract the value of environmental impedance and find it to be in agreement with the expected value of  $\sim 300\Omega$ .

Finally, we characterize our junctions in a magnetic field perpendicular to the graphene sheet. In addition to applying a magnetic field by an external coil, we apply small fields by passing a current along one of the superconducting leads of the junction. This magnetic field modulation of the critical current results in the classical Fraunhofer interference pattern. However, some deviations from this pattern are observed. We attribute these deviations to our sample design, and run simple simulations to support this conclusion.

## 8.2 Future measurements

The critical current through the graphene-based Josephson junction should depend on the Thouless energy  $E_{Th}$ . However, in our previous measurements we were unable to vary  $E_{Th}$  sufficiently to confirm or deny the theoretical predictions for this relationship (Fig 6.3 d). Similarly, we were unable to vary the temperature enough to claim that the critical current is suppressed with temperature according to the SNS theory(28). We have increased the available temperature range by conducting the measurements in a dilution refrigerator (in progress). Unlike the previous measurement, where a single device was made on one graphene crystal, we have to divided a larger graphene sheet into several SNS Josephson junctions of various lengths. As the

Thouless energy is suppressed as  $1/L^2$ , having several devices increases the range of  $E_{Th}$  we can sample.

Our graphene-based SNS Josephson junctions are found to be underdamped at DC. The high quality factor  $Q$  in our junction is attributed to the large capacitance between the superconducting leads coupling through the back gate. Our recent calculations and measurement show that simply terminating the superconducting electrodes as soon as possible after they leave the graphene sheet (thus suppressing  $C$ ) is not sufficient. The low resistance of the Cr/Au electrodes does not isolate the junction and the capacitance of the large bonding pads greatly increases the junction quality factor  $Q$ . The leads contacting the superconducting portion of the junction must be made much more resistive in order to isolate the junction properly and create a truly overdamped junction. In addition to isolation, by having the lead resistance be of the order of the junction normal resistance it is possible to engineer the current-voltage characteristics in the phase diffusion regime, increasing the measured voltage and thus making the measurement more robust(25).

# Bibliography

- [1] H. Kamerlingh Onnes, Leiden Comm. **120b**, **122c**, **124c**, (1911)
- [2] M. Tinkham, *Introduction To Superconductivity* (McGraw-Hill, 1996).
- [3] B.D. Josephson, Phys. Lett., **1**, 251 (1962).
- [4] C.M. Wilson, L. Frunzio and D.E. Prober, IEEE Trans. Appl. Supercond. **13**, 1120 (2003).
- [5] Y. Makhlin, G. Schon, and A. Shnirman, *Scalable Quantum Computers: Paving the Way to Realization* (Wiley-VCH, 2001).
- [6] P.R. Wallace, Phys. Rev. **71**, (9): 622 (1947).
- [7] K. S. Novoselov, D. Jiang, F. Schedin, T.J. Booth, V. V. Khotkevich, S. V. Morozov, and A. K. Geim, PNAS **102**, 10451 (2005).
- [8] A.K. Geim, K. S. and Novoselov, Nature Materials **6**, 183 (2007).
- [9] B. H. Hong, APS March Meeting, W2.00002 (2011).
- [10] S. Bae, H. Kim, Y. Lee, X. Xu, J-S. Park, Y. Zheng, J. Balakrishnan, T. Lei, H. Ri Kim, Y. I. Song, Y-J. Kim, K. S. Kim, B. Ozyilmaz, J-H. Ahn, B. H. Hong, S. Iijima, Nature Nano. **5**, 574 (2010)
- [11] G.W. Semenoff, Phys. Rev. Lett. **53**, 2449 (1984).
- [12] P. Avouris, C. Chen, and V. Perebeinos, Nature Nano. **2**, 605 (2007).
- [13] J. H. Chen, C. Jang, S. Xiao, M. Ishigami, and M. S. Fuhrer, Nature Nano. **3**, 206, (2008).
- [14] A. H. Castro Neto, F. Guinea, N. M. R. Peres, K. S. Novoselov, and A. K. Geim, Rev. Mod. Phys., **81**, 109 (2009).
- [15] J. Martin, N. Akerman, G. Ulbricht, T. Lohmann, J. H. Smet, K. von Klitzing, and A. Yacoby, Nature Physics **4**, 144 (2008).
- [16] O. Klein, Zeitschrift Physik **53**, 157 (1929).

- [17] X. Du, I. Skachko, A. Barker, and E. Y. Andrei, *Nature Nano.* **3**, 491 (2008).
- [18] K. K. Likharev, *Dynamics of Josephson Junctions and Circuits* (Gordon and Breach, 1991).
- [19] Y. M. Ivanchenko and L. A. Zil'berman, *JETP Letters* **8**, 113 (1968).
- [20] Y. M. Ivanchenko and L. A. Zil'berman, *Sov. Phys. JETP* **28**, 1272 (1969).
- [21] V. Ambegaokar and B. I. Halperin, *Phys. Rev. Lett.* **22**, 1364 (1969).
- [22] G. L. Ingold, H. Grabert, and U. Eberhardt, *Phys. Rev. B* **50**, 395 (1994).
- [23] J. M. Martinis and R. L. Kautz, *Phys. Rev. Lett.* **63**, 1507 (1989); R. L. Kautz and J. M. Martinis, *Phys. Rev. B* **42**, 9903 (1990).
- [24] J. M. Kivioja, T. E. Nieminen, J. Claudon, O. Buisson, F. W. J. Hekking, and J. P. Pekola, *Phys. Rev. Lett.* **94**, 247002 (2005).
- [25] P. Joyez, D. Vion, M. Götze, M. H. Devoret, and D. Esteve, *Journal of Superconductivity*, **12**:6, 757 (1999).
- [26] J. T. Anderson and A. M. Goldman, *Phys. Rev. Lett.* **23**, 128, (1969).
- [27] V. Ambegaokar and A. Baratoff, *Phys. Rev. Lett.* **10**, 486 (1963); T. van Duzer, and C. Turner, *Principles of Superconductive Devices and Circuits* (Prentice-Hall, 1999).
- [28] P. Dubos, H. Courtois, B. Pannetier, F. K. Wilhelm, A. D. Zaikin, and G. Schön, *Phys. Rev. B* **63**, 064502 (2001).
- [29] H.J. Fink, *Phys. Rev. B* **14**, 1028 (1976).
- [30] X. Du, I. Skachko, and E. Y. Andrei, *Phys. Rev. B* **77**, 184507 (2008).
- [31] H. B. Heersche, P. Jarillo-Herrero, J. B. Oostinga, L. M. K. Vandersypen, and A. F. Morpurgo, *Nature* **446**, 56 (2007).
- [32] D. Jeong, J-H. Choi, G-H. Lee, S. Jo, Y-J. Doh, and H-J. Lee, *Phys. Rev. B* **83**, 094503 (2011).
- [33] P. Blake, E.W. Hill, A.H.C. Neto, K.S. Novoselov, D. Jiang, R. Yang, T.J. Booth, and A.K. Geim, *App. Phys. Lett.* **91**, 063124 (2007)
- [34] I. Jung, M. Pelton, R. Piner, D. A. Dikin, S. Stankovich, S. Watcharotone, M. Hausner, and R. S. Ruoff, e-print arXiv:cond-mat/0706.0029.; C. Casiraghi, A. Hartschuh, E. Lidorikis, H. Qian, H. Harutyunyan, T. Gokus, K. S. Novoselov, and A. C. Ferrari, e-print arXiv:cond-mat/0705.2645.

- [35] A. C. Ferrari, J. C. Meyer, V. Scardaci, C. Casiraghi, M. Lazzeri, F. Mauri, S. Piscanec, D. Jiang, K. S. Novoselov, S. Roth, and A. K. Geim, *Phys. Rev. Lett.* **97** 187401, (2006).
- [36] B. Huard, N. Stander, J. A. Sulpizio, and D. Goldhaber-Gordon, *Phys. Rev. B* **78**, 121402 (2008).
- [37] F. Xia, V. Perebeinos, Y. Lin, Y. Wu, and P. Avouris, *Nature Nano.* **6**, 179 (2011).
- [38] *Low Level Measurements Handbook* (Keithley).
- [39] H.W. Ott, *Noise Reduction Techniques in Electronic Systems* (Wiley-Interscience, 1988).
- [40] H. C. Meijer, C. Beduz, and F. Mathu, *J. Phys. E: Sci. Instrum.*, **7**, 424 (1974)
- [41] For a review, see *e.g.* S. De Franceschi, L. Kouwenhoven, C. Schönberger, and W. Wernsdorfer, *Nature Nano.* **5**, 703 (2010).
- [42] F. Miao, S. Wijeratne, Y. Zhang, U. C. Coskun, W. Bao, and C. N. Lau, *Science* **317**, 1530 (2007).
- [43] C. Ojeda-Aristizabal, M. Ferrier, S. Gueron, and H. Bouchiat, *Phys. Rev. B* **79**, 165436 (2009).
- [44] H. Courtois, M. Meschke, J. T. Peltonen, and J. P. Pekola, *Phys. Rev. Lett.* **101**, 067002 (2008).
- [45] T. Tsuneta, L. Lechner, and P. J. Hakonen, *Phys. Rev. Lett.* **98**, 087002 (2007).
- [46] Using the exponential approximation to the full formula of Ref. 17 is estimated to produce an error of not more than 30% at the highest temperature and the lowest  $E_J$ .
- [47] We estimate that the phase gradient created in the leads by  $I_L$  is small, and does not induce a significant phase shift along their length. Moreover, the effect of such phase shift, linear along the length of the leads, would be similar but much smaller than the effect of magnetic flux, which also grows linearly along the length of the leads.
- [48] V. M. Krasnov, T. Golod, T. Bauch, and P. Delsing, *Phys. Rev. B* **76**, 224517 (2007).
- [49] I. V. Borzenets, U. C. Coskun, S. J. Jones, and G. Finkelstein, *Phys. Rev. Lett.*, **107**, 137005 (2011).

- [50] S. L. Miller, K. R. Biagi, J. R. Clem, and D. K. Finnemore, *Phys. Rev. B*, **31**, 2684 (1985).
- [51] T. Gaber, E. Goldobin, A. Sterck, R. Kleiner, D. Koelle, M. Siegel, and M. Neuhaus, *Phys. Rev. B*, **72**, 054522 (2005).
- [52] E. Goldobin, A. Sterck, T. Gaber, D. Koelle, and R. Kleiner, *Phys. Rev. Lett.*, **92**, 057005 (2004).
- [53] C. Chialvo, I. C. Moraru, D. J. Van Harlingen, and N. Mason, *arXiv:1005.2630v2* (2010).

# Biography

## 1. Brief Description:

Ivan Valerievich Borzenets was born on April 21, 1984 in Kharkov, Ukraine. In 1995 he immigrated with his family to San Francisco, California.

Ivan received a B.S. degree in Engineering Physics from the University of California, Berkeley in 2006. During his time in Berkeley, he worked as an undergraduate lab assistant at research groups of Prof. Frances Hellman in Physics, and Prof. Ted van Duzer in Electrical Engineering. In addition, he has spent a summer working for the Prof. Dan Prober group at the Yale University, Applied Physics Department.

Ivan received a graduate education at Duke University where he obtained an M.S. in Electrical and Computer Engineering in 2011, and a Ph.D. in Physics in 2012. His Ph.D. work was lead by Prof. Gleb Finkelstein.

## 2. List of publications:

I. Borzenets, U. Coscun, S.Jones, G.Finklestein, Phase diffusion in graphene-based Josephson junctions, Physical Review Letters (2011)

I. Borzenets, U. Coscun, H. Mebrahtu, G. Finkelstein, Pb-graphene-Pb Josephson junctions: characterization in B field, Submitted to IEEE Journal of Applied Superconductivity, (March. 2012)

I. Borzenets, I. Yoon, M. Prior, B. Donald, R. Mooney, G. Finkelstein, Ultra-sharp metal and nanotube based probes for applications in scanning microscopy and neural recording. Journal of Applied Physics, (2012)

H. Mebrahtu, I. Borzenets, Yu. Bomze, and G. Finkelstein, Resonant Level in Dissipative Environment: a Quantum Phase Transition in an Artificial Quantum Impurity, Submitted to Science, (Nov 2011)

Yu. Bomze, I. Borzenets, H. Mebrahtu, A. Makarovski, H. U. Baranger, and G. Finkelstein, Two-Stage Kondo and Level Spectroscopy of the Kondo Box in Carbon Nanotube, Physical Review B (2010)

P. Li, P. M. Wu, Yu. Bomze, I. Borzenets, G. Finkelstein, A. M. Chang, Retrapping Current, Self- Heating, and Hysteretic Current-Voltage Curves in Ultra-Narrow Superconducting Aluminum Nanowires, Physical Review B (2011)

P. Li, P. M. Wu, Yu. Bomze, I. Borzenets, G. Finkelstein, A. M. Chang, Switching currents limited by single phase slips in one-dimensional superconducting Al nanowires, Physical Review Letters (2011)

Y. Bomze, H. Mebrahtu, I. Borzenets, A. Makarovski, G. Finkelstein Resonant tunneling in a dissipative environment, Physical Review B (2009)

3. List of presentations:

I. Borzenets, Ulas Coskun, Gleb Finkelstein, Pb-graphene-Pb junctions: phase diffusion and Fraunhofer pattern, Oral Presentation, EP2DS19/MSS15, 2011

I. Borzenets, Ulas Coskun, Gleb Finkelstein, S-N-S junction formed by graphene with lead (Pb) contacts. Oral Presentation, American Physical Society, March Meeting 2011

I. Borzenets, Y. Bomze, H. Mebrahtu, G. Finkelstein, "Kondo Box in a Carbon Nanotube", Oral Presentation, American Physical Society, March Meeting 2010

I. Borzenets, H. Mebrahtu, U. Coskun, M. Prior, A. Zhukov, G. Finkelstein, Low Temperature Conducting Probe Microscopy of Carbon Nanotubes, Poster, American Physical Society March Meeting 2009

4. List of awards:

G.P. Nano (Nanoscience) fellowship, Duke University, 2006

Fritz London fellowship, Duke University, 2011

5. Future plans:

Ivan Borzenets has accepted a postdoctoral position at Prof. Tarucha's group in the University of Tokyo, Japan. He is tasked with designing a superconducting graphene based cooper-pair splitter.